From the Klinik für Radiologie und Neuroradiologie
(Director: Prof. Dr. med. O. Jansen)
At the University Medical Center Schleswig-Holstein, Campus Kiel
at Kiel University

Movement correction by object recognition-based anatomical tracking in functional magnetic resonance urography (fMRU) – proof of principle

Dissertation
to acquire the doctoral degree (Dr. med.)
at the Faculty of Medicine

at Kiel University

presented by

Andreas Holmberg

from Brännkyrka

Kiel 2017

1st Reviewer: Priv.-Doz. Dr. Jörg D. Moritz
2nd Reviewer: Prof. Dr. K.-P. Jünemann
Date of oral examination: 28.09.2018
Approved for printing, Kiel, 23.07.2018

Signed: Prof. Dr. Johann Roider

(Chairperson of the Examination Committee)

Table of contents

1. Introduction

1.1 Anatomy and function of the kidney

Anatomy

The kidneys are located in the retroperitoneal space in the abdominal cavity where the left kidney lies further cranial than the right. Both kidneys communicate from below with the diaphragm, the right kidney located posterior to the liver and the left kidney posterior to the spleen. From the abdominal aorta both kidneys receive an estimated 20% - 25% of cardiac output, necessary for upholding the renal filtration function (1). Following the blood flow on its path along the blood vessels of the kidney explains in which order the different compartments are made visible with contrast agent. From the renal arteries the segmental and later interlobar arteries originate, followed by the arcuate arteries spanning the cortex space between the pyramids. Connecting to the kidney functional unit, the glomeruli, urine is transported by way of the pyramids converging into the calixes and lastly kidney pelvis(2). Thus the kidneys functional structures can be divided into cortex, pyramids (medullae) and calix.

Function

Kidney functions can be divided into three categories: homeostasis, filter function and hormone production. Regulation of inner environment that is homeostasis includes balancing electrolytes like sodium or potassium, maintaining appropriate blood pressure and keeping the pH-level as close to 7.4 as possible (3). Another important function is the ability to filter unwanted substances from the body, such as urea and ammonium. Lastly communication with other systems of the body is maintained through production and excretion of hormones such as calcitriol, renine and erythropoetine, further influencing calcium household, blood pressure and oxygenation by regulating red blood cell count.

1.2 Assessment of renal function

1.2.1 Clinical and laboratory assessment

In a laboratorial and clinical setting, kidney function can be quantified and assessed by examination of either urine or blood samples. Visually the urine can be examined in properties

of color, indicating a rough estimate of urine concentration, and clarity, showing possible signs of infection or presence of substances not filtered correctly. An efficient method of gathering more information to base a diagnosis on can be done with urine sticks. Depending on type of urine stick, several parameters can be measured simultaneously in a relative short time span, indicators changing color accordingly. Properties like glucose, protein, pH, blood cells, ketones, bilirubin and nitrates can be estimated with high precision (4).

Examining a urine sample in a laboratory with appropriate equipment may sometimes be preferable. Normal urine pH ranges from 4.6 to 8, with a tendency towards a more acidic pH of about 6 and can help diagnosing diseases like urinary tract infections, diabetic ketoacidosis and kidney failure (3). Presence of glucose in urine is indicative of kidney dysfunction, as glucose normally is reabsorbed in the proximal tubule. Exceeding this renal threshold of glucose (RTG) leads to glucose in the urine and is often caused by elevated blood glucose levels due to diabetes mellitus (3). Normal protein secretion per day can amount to 150 mg (5). A simple way of obtaining the protein excretion level is to collect the urine for 24 hours. Being a time-consuming test, a quicker and more efficient method is to calculate the protein/creatinine ratio (PCR) which should not exceed 15 mg/mmol (6), otherwise indicating proteinuria.

GFR

Quantification of kidney function in is often done through measurement of the creatinine level in urine and blood samples from the patient. This is a standard test in most medical facilities and correlates with the kidneys glomerular filtration rate (GFR), indicating the current state of kidney functions (7). The GFR formula for any freely filtered substances is defined as (3):

$$GFR = \frac{Urine\ Concentration\ x\ Urine\ Flow}{Plasma\ Concentration}$$

and requires both serum and urine concentrations levels of creatinine obtained from a 24 h collection (8). To be able to estimate the GFR from blood samples the formula from Cockroft and Gault is used, defined by (3):

$$eC_{Cr} = \frac{(140 - Age)x\ Mass\ (in\ kilograms)x\ [0.85\ if\ Female]}{72\ x\ Serum\ Creatinine\ (in \frac{mg}{dL})}$$

eC_{Cr}: Estimated clearance rate for creatinine through Cockroft and Gault formula

This method bases its GFR estimation on predefined values of urinary creatinine excretion per kilogram body weight according to age (9). A modified and more accurate formula is the Modification of diet in renal disease equation (MDRD) which contrary to the CG formula does not tend to overestimate GFR (8).

$$eGFR = 186 * Serum\ Creatinine^{-1.154} * Age^{-0.203} * [1.212\ if\ Black] * [0.742\ if\ Female]$$

eGFR: Estimated glomerular filtration rate through MDRD formula

Nuclear medicine

Nuclear imaging takes advantage of the fact that radioactive isotopes are transported to regions in the body with increased metabolism when coupled with a suitable tracer. Depending on the property and metabolism of said tracer, the function of an organ or tissue can be analyzed. One of the most commonly used radioisotopes is Technetium (^{99m}Tc), the activity of which can be measured by a gamma camera. To get the radioisotope to its intended destination it has to be coupled with a tracer. In renal imaging popular tracers include MAG3 (mercaptoacetyltriglycine) and DMSA (dimercaptosuccinic acid). MAG3 has a quick renal transit time where 90 % of applied dose is found in the urine three hours post injection, making it an ideal agent for assessment of renal tubular functions including uptake and excretion (10). DMSA finds its use when searching for signs of kidney cortical lesions as it is actively absorbed in the proximal and distal tubule, thereby representing cortical mass. Additionally information can be extracted regarding relative renal mass and gross anatomy. In comparison, DMSA has a slower renal transit time where 40-65% of applied dose can be found in the cortex two hours post injection, making prolonged imaging possible but with the downside of increased radiation dose (10). Normal results of a ^{99m}TC-MAG3 test however does not always necessitate additional diagnostics with the more dose-intensive ^{99m}TC-DMSA method, as the previous has been shown to deliver adequate information regarding kidney function, thus leading to reduced radiation exposure (10).

The methods available in nuclear medicine such as PET and scintigraphy offer very good imaging results when functional properties of metabolism in the body have to be examined. Trace amounts of metabolites on a picomolar level can be measured resulting in detailed functional imaging (11). This obvious advantage is strongly contrasted by its deficiency in conveying spatial resolution, a problem that is addressed by hybrid imaging where different modalities of radiological imaging are combined to deliver both functional and morphological imaging in one test. Examples include PET/CT and PET/MRT, increasing medical diagnostic accuracy in fields such as oncology, cardiology and endocrinology.

1.2.2 Functional magnetic resonance urography (*f*MRU)

1.2.2.1 Theory

Following segment pertains to the general theory of MRI technology.

Electromagnetism and signal-to-noise ratio

Magnetic resonance imaging (MRI) utilizes the magnetic properties of hydrogen atoms in water molecules to produce slice images of the human body. These hydrogen atoms possess an intrinsic angular momentum called spin, which generates a dipole magnetic field with an individual vector orientation. The individual vector orientation for each hydrogen atom, also called spin polarization, is regarded in relationship to its alignment with a given direction. An external magnetic field, as produced in a MRI machine, is called the primary magnetic field (B_0) and can influence the orientation of these spin vectors, aligning the dipoles in a parallel or antiparallel direction (low or high energy states) along the primary field B_0. At body temperature, the Boltzmann distribution predicts near equilibrium between low and high energy states, with a small majority in favor of the lower energy state. This longitudinal magnetization results in a net magnetic vector along a z-axis, the same direction as the primary field. The protons rotate around the z-axis in a manner called precession, at a frequency proportional to the strength of the magnetic field. Further components of the MRI machine are coils that add a gradient to B_0. The influence of the gradient coils on the primary magnetic field occurs in direction of the x-, y-, and z-plane which alters the precession rates of the protons, allowing for identification of individual slices based on precession frequencies.

Thus far, the primary magnetic field B_0 as well as a gradient have been established. To be able

to produce images, a third component is required to emit and receive radio frequency pulses, the radio frequency coils. Energy from the rf-pulse is absorbed by the proton which flips to a higher energy state, leading to a decrease in longitudinal magnetization. Secondly, the protons start to precess in phase in the transverse plane, called transverse magnetization. The time it takes to resume normal longitudinal magnetization is called T1-relaxation time, correspondingly the decay of transverse magnetization is called T2-relaxation time. T1-relaxation time depends on the protons shift from a higher to a lower energy state. T2-relaxation time depends on the de-phasing or de-synchronization of proton precession. Different tissues have hydrogen atoms in varying concentrations and molecular constellations, thus possessing individual T1- and T2-relaxation times which can be used to distinguish structures in the human body (12) (13).

The fourth and last component of the MRI machine is a high performance computer capable of performing complex calculations converting the analogue radiofrequency signal into digital data. By usage of Fourier Transformation the data can be mapped into images and displayed on a monitor for interpretation. Image quality depends in part on gradient magnetic fields with varying strength in stationary (B_0) fields, where two of the most commonly used field strengths are 1.5 Tesla and 3 Tesla. Doubling the strength from 1.5 T to 3 T results in a change of the signal-to-noise-ratio from S0/N0 = 1 to S1/N1 = 2, meaning a doubling of the S/N-ratio and thereby an increase in spatial and temporal resolution (14).
Despite obvious advantages, certain precautions have to be taken. The specific absorption rate limits still have to be respected to not exaggerate the energy deposition in the body. There are different approaches available to circumnavigate these obstacles. Reducing the energy absorption can be done by increasing the relaxation time between pulses, slab thickness can be increased and changes to pulse sequences can be made. These changes have consequences in that the total scan time is prolonged and anatomical detail may be reduced (14).

Following segment pertains to the theory of fMRU technology.

T2

Magnetic Resonance Urography can be divided into two categories: Static-fluid urography and excretory urography (15). Static-fluid urography uses T2-weighted sequences where stationary fluids with high amounts of water give a signal intense image. This means that compartments where fluids are collected can be visualized, including kidney, ureter and

bladder. Obtaining these images does not require any contrast agent which is made possible by using the long T2 relaxation time of water in sequences like RARE (rapid acquisition with relaxation enhancement) or the faster HASTE (half-Fourier acquisition single-shot turbo spin echo) sequences(16). The acquired images can thus be used to evaluate anatomic anomalies like urinary tract obstruction and dilation, as they would impede the flow of urine. This method can also be used on patients with limited renal function as the excretory capabilities of the kidney are neither measured nor necessary for evaluation (15).

T1

Anatomic structures that are smaller or narrower in size, and therefore hold small amounts of water, can be visualized by intravenous injection of contrast agent. As the contrast agent is excreted through the kidneys, it will mix with fluid in water-filled structures on its path through the urinary tract, thus making them visible. Combined with sufficient hydration and diuretics like furosemide, it becomes possible to examine non-distending urinary tracts. If the contrast agent is too concentrated as a result of insufficient dilution by diuretics or hydration, the T*-effect can cause signal loss (17). The sequence is then recorded 5-8 minutes post injection. This is done in T1-weighted sequences and is also used to quantify the excretory function of the kidney (16). Possible T1-weighted sequences include 3D gradient-echo sequence, with optional fat suppression (ureters), VIBE (Volumetric Interpolated Breath hold Examination), FAME (Fast Acquisition with Multiphase Efgre 3D), THRIVE (T1-weighted High-Resolution Isotropic Volume Examination) and LAVA (Liver Acquisition with Volume Acceleration) (15).

Temporal and spatial resolution

Time frame

Scan time length of MR Urography varies depending on selected imaging sequence, desired information level and anatomic region. Leyendecker et. al. presented a list of possible imaging sequences intended as a comprehensive all-in-one protocol for MR Urography with scan times between 30 and 60 minutes (15). While a single-shot fast spin-echo image as part of a static fluid T2-weighted sequence will take about two seconds to acquire, a T1-weighted image for evaluation of renal excretory function may take 20-30 seconds (15)(16). Compared to CT, where a full-body scan is completed in a matter of seconds, MR Urography with its estimated scanning time closer to an hour clearly limits the frequency of examinations. This,

on the other hand, is still more time efficient than the scintigraphic alternative where the actual scan time can be realized 30 minutes, preparations however include a waiting time of several hours giving the injected tracer time to accumulate in the kidneys (18).

Because of the relative long acquisition times in MR Urography, image artifacts from the patient's motion and breathing might have a noticeable impact on image quality. Different methods have been developed to counter this fact, including breath-holding during the scan and imaging done by respiratory triggering, whereas the former has been shown to deliver higher quality images when depicting the pelvicalyceal systems and the latter when viewing the ureters (19).

Comparison to CT

Although MR Urography yields images with lower spatial resolution than CT imaging, one of the benefits lie in generation of images with superior spatial contrast resolution (16). As MR Imaging is based on the electron spins of the hydrogen atoms, the tissue intensity varies with hydrogen concentration and can therefore better distinguished contrast variations than a CT scan, where mere density is detected. Unfortunately the extreme radiation load from CT imaging prevents it from becoming a real alternative in terms of functional imaging of the kidneys. When pure morphological imaging is concerned each modality has its advantage, maximizing diagnostic information when combined. For instance, while detection rate of bladder carcinoma is slightly elevated when using CT, the staging of bladder carcinoma is more successful with MR urography, as variations in vesical tissue are more easily recognized (20), (21). This example manages to highlight MR scan properties: because of the MR scanners lower spatial resolution, detection of small anomalies can be difficult. At the same time, knowing the location of said anomaly and with the prerequisite of it being soft-tissue-based, correct sequences may allow for more specific differentiation. Naturally, problems arise when the desired goal is to scan for non-tissue structures. Most evidently this proves a difficult obstacle when the differential diagnosis for renal calculi is to be ascertained. Though diagnosis of ureteral calculi is seen as one of the weaknesses of MR Urography, excretory techniques still manage to reach detection rates of 90% and are more successful at detecting other causes of urinary tract obstruction than CT (16).

Comparison to Nuclear imaging

In contrast to the relation between CT and MR Urography in terms of which method provides

the most efficient way of diagnosing renal diseases, both morphologically and functionally, nuclear imaging takes a more obvious position indication wise. Even though physiological differences exist when it comes to the body's elimination of MRI contrast agent and the tracers of nuclear medicine, where gadolinium is only filtered while nuclear tracers are both filtered and actively excreted, this fact has no impact on our comparison. Where renal nuclear imaging performs in delivering information about kidney functionality, it does not suffice when it comes to anatomical and morphological detail, lacking in spatial resolution (17), (22). MR Urography thus shows benefits in that morphological data can be presented in both T1- and T2-weighted sequences, as well as delivering information about renal excretory function with Gadolinium enhanced T1-weighted sequences, all without exposure to radiation (15), (16). In a study performed by Hadjidevov et. al. in 2011, they summarized their findings by stating:

"We consider images quality of the kidney and the collecting system to be superior with MR urography in comparison to ultrasound and DTPA renogram in all 96 cases." (22)

Patlak score/plot

Intravenous application of Gadolinium contrast agent is necessary to properly examine kidney excretory functions. For image evaluation, a linear relationship between contrast agent concentration and depicted image signal intensity has to be fulfilled (23). This linearity depends on which MR scanner is used as well as the combination of scanning protocol and flip angle, exemplified by the numerous sequences used for kidney function evaluation by Nikken and Krestin et al (17). Failing to establish said linearity, the necessary Patlak equations cannot be solved and the data will not be retrievable from image analysis (23). Additionally, the concentration and flow of Gadolinium does influence image outcome in what is called the T2 shortening effect. In T1-weighted sequences, high concentration of Gadolinium increases the T2 effect and results in lower signal intensity in collecting compartments, effectively negating the purpose of T1 excretion imaging (24). Therefore a maximum flow and concentration has to be defined and not exceeded so that the contrast agent is diluted sufficiently over time, maintaining the T1 effect with a nearly linear relationship between Gadolinium concentration and signal intensity (25).

To extract data concerning kidney function the Patlak-Ruthland method is used which describes the interaction of pharmacokinetic substances between different compartments in

the body (26). In this case the concentration and flow of Gadolinium contrast agent from the vascular space of the aorta to the nephron space of the renal parenchyma can be analyzed (27). In the end the data is graphically presented in a Patlak plot in the form of a slope proportional to renal clearance, indicating GFR (28).

The intensity changes in the regions of interest over aorta and renal parenchyma are measured. The ratio between signal intensity in aorta and kidneys is defined on the y-axis, meaning a high concentration in the aorta relative to the kidney (as it is in the beginning of analysis) yields a low ratio value (Equation).

$$\text{y-axis} = \frac{Kidney_{Concentration}(Enhancement\ curve)}{Aorta_{Concentration}(Enhancement\ curve)}$$

As the Gadolinium is transferred into the renal parenchyma the ratio increases. At some point this upward trending slope is going to flatten out, indicating a shift in Gadolinium concentration as it is filtered into the calyceal system. As one of the requirements for this model to work, the Gadolinium may not leave the renal parenchyma while measurements are performed. Therefore the slope that is calculated with linear regression is defined between the starting point of measurement and the point where Gadolinium is first seen leaving the renal parenchyma (23). The x-axis not only denotes time but also incorporates following calculations:

$$\text{x-axis} = \frac{\int Aorta_{Concentration}(Enhancement\ curve)}{Aorta_{Concentration}(Enhancement\ curve}$$

Combined with the requirement that the rate of change in Gadolinium concentration is constant in regard to its volume, the coefficient of the slope signifies the Patlak number which can be used in further calculations to estimate GFR (23). Resulting GFR values should not be taken too seriously though as studies indicate it being a much too unreliable method, it does however visualize the overall function of the kidneys, especially in relation to each other (28), (29).

1.2.2.2 Areas of application and indications

While MRI imaging is no longer an experimental method of acquiring necessary information about organ anatomy and function, new areas of application are discovered and refined in an upward pointing trend. The reasons are numerous, ranging from soft tissue image quality to limited side effects from the examination itself (16). One of the obvious advantages to some of the previous imaging techniques like CT and the now relatively obsolete intravenous urography is the absence of ionizing radiation. This makes it a preferred diagnostic tool in areas where sensitivity or consequence of radiation can be regarded as elevated. Specialties included are those which are predominated by children like pediatrics and neonatology, pregnant patients in gynecology, as well as breastfeeding mothers. Patients who are the receivers of multiple imaging examinations as part of their treatment plan may also benefit from lowered exposure. Compared to nuclear imaging like PET and scintigram, functional MR Urography may, considering the risk for nephrogenic systemic fibrosis induced by Gadolinium contrast agent, offer an additional alternative to patients with reduced renal function where prolonged retention of radiating substances would otherwise lead to increased exposure.

Urolithiasis

Calcium-based calculi count as one of the most common forms and cause of urolithiasis (30). While sonography still counts as the primary imaging modality for urolithiasis in children, MR imaging shows promise in certain cases (31). In MRU imaging the calculi itself will be represented by signal void in both T1 and T2 weighted sequences, direct and certain differentiation to other causes thus cannot be made based on these findings. What can be seen are the secondary effects of urolithiasis in the form of obstructions and signs of infection (30). Using T2 weighted sequences, static-fluid images can be obtained where stationary amounts of urine will be contrasted. The additional application of gadolinium contrast agent and diuretics like furosemide would increase both fluid intensity and flow, thereby bringing added information for evaluation (32). Compared to iodine-based contrast agents used in computer tomography, gadolinium is not nephrotoxic and MR urography therefore becomes an ideal method of safely examining patients where obstruction is the main suspicion (33). Retention of the contrast agent has few side effects on the kidneys, which further facilitates patient with already poor renal function or are at risk for allergic reactions against iodine.

Urothelial Carcinoma

There are several imaging techniques available to help in the diagnosis of both upper and lower urinary tract malignancies. For the upper urinary tract, urography with CT and MR as well as retrograde and excretory urography can be used to detect transitional cell carcinoma (20). Highest sensitivity/specificity was shown for the CT urography with 96%/99% accuracy compared to MR urography with 69%/97% accuracy. For the lower urinary tract malignancies, CT and MR cystography along with ultrasonography are common, CT cystography once again showing highest accuracy with 94%/98% sensitivity/specificity compared to MR cystography 91%/95% (20). Where CT techniques demonstrate superior accuracy when detecting urinary tract malignancies, MR techniques still maintain distinct advantages. Absence of radiation enables multiple imaging sequences where inherent susceptibility to motion artifacts and lower spatial resolution would distort image quality (34). For upper urinary tract imaging, MR urography becomes viable and indicated in patients with contraindication to regular CT urography, including renal insufficiency or allergies to contrast agents (34). Bladder carcinomas can be more accurately staged with MR imaging compared to CT, as MR offers a higher soft-tissue contrast resolution (21).

Vesicoureteral reflux

Among the most established methods for diagnosing vesicoureteral reflux are voiding cystourethrography with fluoroscopy and radionuclide cystography, while sonographic techniques are becoming increasingly popular (35)(36). Obvious downside being radiation exposure to the patient, radiation-free methods like voiding urosonography and MR voiding cystograms have emerged in order to diagnose reflux. While voiding urosonography presents a more accessible technique than MR imaging, MR voiding cystograms show high precision levels with a sensitivity/specificity accuracy of 90%/96% (37). Imaging is performed using T2-weighted sequences, making it a non-invasive method where transurethral catheterization and intravesical instillation of contrast agent is omitted (37). As vesicoureteral reflux is common in children, the mantra as low as possible achievable signifies the importance of reducing complications that could follow examination. MR imaging represents many of these qualities, but not without its own obstacles yet to overcome. Long examination time may require sedation of non-compliant children and supine position while voiding is problematic. Application of diuretic and hydration may cause increased antegrade ureteral flow, influencing examination outcome (37).

Congenital anomalies

While ultrasonography still remains the standard for diagnosing renal congenital anomalies in pre- and postnatal children, MR imaging could become a valuable addition to diagnostics (38)(39). MR imaging finds its use in pediatrics with patients that are born with urologic anomalies. Anomalies with high prevalence like ureteropelvic obstruction, megaureters and megacalycosis are detectable as well as less frequent anomalies being renal malformation in the form of hypoplasia, horseshoe form and rotation, including cystic anomalies (22). These can be identified on T2-weighted sequences where anatomy is of primary interest. Using T1-weighted images, renal excretory function can be measured with the help of gadolinium contrast agent. Presence of duplicated ureters can be visualized and symptoms of obstruction like hydronephrosis and megaureter can be differentiated by observation of delayed excretion of contrast agent into collecting systems (22). MR imaging shows high sensitivity when diagnosing urinary tract obstructions and dilations, approaching an accuracy of nearly 100% and equally effective at diagnosing pediatric uropathies when compared to ultrasonography, intravenous urography and nuclear scintigraphy (40) (16).

Kidney donors/OP

With over 1600 transplantations performed 2012 in Germany, the kidney is the most donated and transplanted organ today (41). Considering the frequency of transplants, reliable methods have to be used to assess both recipient and donor kidney function to maximize successful outcome of surgery. Even though live organ donors make out the lesser category of transplants, the tendency is pointing upward and brings with it improved long time survival (42). With gadolinium enhanced MRU, it is possible to correctly visualize renal collecting system and ureters, together with accurately estimating 24-hour creatinine clearing and thus kidney GFR, essential for assessment of viable transplants (42). El-Diasty et al conclude:

"Therefore, we recommend Gd-enhanced dynamic MRI as a single imaging method for assessing potential live-kidney donors."

Post op imaging and follow up assessment can give indications of complication in form of renal function loss and rejection of transplanted kidney (43). Signs of rejection include increased levels of creatinine in plasma, decreased urine output and hypertension (43). While laboratory tests and ultrasonography to measure kidney perfusion will yield information about kidney function, MR imaging offers a method of visualizing the collecting system (44). It is

possible to identify ureter stricture and stenosis by T2-weighted sequences, as well as parenchymal deficiencies of the renal cortex in T1-weighted sequences with contrast agent (43).

Contra indications

Kidney disease

When conducting T1-weighted MRU to measure renal excretory function, Gadolinium based contrast agent is used. It follows that MRU scans made to determine renal excretory function will be dependent on the patient's ability to properly eliminate said agent, which can be achieved by measuring GRF prior to examination, indicating renal clearance. The main reason for this is to minimize risk to induce Nephrotic systemic fibrosis, which has been linked to application of gadolinium based contrast agent in patients with reduced renal function or insufficiency (45). The European Society of Urogenital Radiology (ESUR) divides the patients at risk into three categories: not at risk, lower risk and higher risk for NSF. Deemed as not at risk are patients with a GFR greater than 60 ml/min. Lower risk includes patients diagnosed with chronic kidney disease (CKD) stage 3, meaning a measured GFR value between 30 and 59 ml/min. High risk patients are defined as having been diagnosed with CKD stage 4 or 5, indicating a GFR below 30 ml/min. Also included in this group of high risk patients are patients on dialysis and those suffering from acute renal insufficiency (46).

There are three Gadolinium based contrast agent have the highest risk of inducing NSF in at risk patients: Gadodiamide (Omniscan®) (incidence 3-18%), Gadopentetate dimeglumine (Magnevist® plus generic products) (incidence 0.1-1%) and Gadoversetamide (Optimark®) (incidence unknown). Contra indications for these agents are patients with a GFR below 30 ml/min (CKD 4 or 5), dialysis, acute renal insufficiency, pregnant women and neonates (46).

Hypersensitivity/Allergies

Even though Gadolinium substrates are regarded as relatively safe, allergic reactions to Gadolinium contrast agents always have to be calculated into the overall risk when conducting MRU scans. Studies have reported immediate hypersensitivity reactions towards MR contrast agents having an incidence of 0.079%, divided between female (0.098%) and male (0.058%) patient groups (47). Thus, patients who do not experience hypersensitivity reactions when exposed to contrast agent for the first time are not guaranteed to be reaction free in the future. Multiple exposures however do increase incidence rates for immediate

hypersensitivity reactions with an incidence rate of 0.137% for two exposures and 0.171% for three exposures (47). If a patient has previously experienced hypersensitivity reaction toward Gadolinium based contrast agents the recurrence rate becomes 30% (47).

Foreign bodies

Patients in possession of foreign material in their bodies have to observe safety regulations regarding interactions between ferromagnetic implants and the magnetic forces of an MRI scanner. These implants may stem from a wide selection of procedures: pacemaker implantation in cardiology, prosthetics in orthopedics, aneurysmal clips from neurosurgery. Risks include implant dislodgement, induction of heat and malfunction of electrically active devices such as pacemakers (48). If possible, foreign objects should be removed prior to MR examination to reduce risk of patient injury, implant malfunction and prevent damages to the MR scanner itself. Even if most implants used today are made from titanium which is compatible with MR scanners, special attention has to be given patients that come from regions of war (49).

1.2.2.3 Radiation dose and contrast agent

One of the many benefits of MR Urography that is reiterated in almost every scientific paper on the matter is the absence of radiation. Except from ultrasonography which utilizes sound waves and therefore does not emit any gamma radiation, MR Urography alone is capable to asses both renal morphology as well as functionality without residual contamination. Examinations in nuclear medicine influence radiation load by means of tracers accumulating in the kidneys. Radiation doses from radiography are smaller than those from CT-scans, but the load is still not insignificant. In *Table 1* some of the most common procedures in radiology and their effective dose are presented for comparison (50).

Table 1: Effective Dose of selected procedures.

Procedure		**Effective Dose (mSv)**
Renogram	99mTc-MAG3	2
Renogram	99mTc-DTPA	2
Renal Cortical Scintigraphy	99mTc-DMSA	3
CT Abdomen/Pelvis		10
Radiography Abdomen		< 1
Natural background radiation (per year)		3

1.2.2.4 Measurement of kidney function

Various imaging methods can be used by themselves, but yield more data when combined together. Images are taken pre and post injection of contrast agent, giving information about both anatomic structure and kidney function. Leyendecker et. al. presented an overview of the most commonly used techniques for MR urography in 2008 (15). In 2010 Khrichenko and Darge showed how they adapted a MRU scanning process based on the recommendations from Gratan-Smith et.al, which outline the scanning procedure in children (23).

Preparations

Before MRU scanning can commence, certain precautions and measures need to be taken to accommodate optimal examination conditions. The application of contrast agent requires the patient to be adequately hydrated, as the contrast agent may not exceed a certain level of concentration. Further facilitating this dilution is the use of diuretics in form of furosemide, which also increases kidney excretory functions so that optimum evaluation of acquired images can be made. Morphological sequences are made immediately post injection of furosemide with an ideal timeframe of 15 minutes until functional sequences are initiated. Increased diuresis makes bladder catheterization a logical next step, removing concerns of over distending the bladder as well as unnecessary interruption of the scanning procedure. In patients with limited compliance, especially younger children, sedation may be necessary to reduce motion artifacts.

Pre-contrast

T2-weighted static-fluid images are taken pre injection and give an overview of the structures that are to be examined. The appropriate angle has to be found where the longitudinal axes of the kidneys are aligned on an oblique coronal plane. Possible scan protocols include thick-

slab single-shot fast spin-echo, half-Fourier rapid acquisition, single-shot fast spin echo, single-shot turbo spin-echo as well as 3D representations by T2-weighted fat-saturated sequences (23), (15).

Post-contrast

For the post-contrast images, Gadolinium-DTPA in a dose of 2-20 ml at a concentration of 0.1 mmol/kg is injected at a maximum flow of 0.25 ml/s. During the next 15 minutes, a dynamic scan is repeated using a 3D T1-weighted gradient echo sequence including fat suppression by saturation, which increases ureter visibility. Sequences include volumetric interpolated breath-hold examination (VIBE), liver acquisition with volume acceleration (LAVA), fast acquisition with multiphase Efgre 3D (FAME) and T1-weighted high resolution isotropic volume examination (THRIVE) (23), (15). Depending on the desired level of information, a MRU scan will take between 30 and 60 minutes to complete, granted necessary preparations are made.

Table 2: Overview of MRU imaging Protocols.

Pre-contrast	**Post-contrast**
- Thick-slab single-shot fast spin-echo	- Fast Acquisition with Multiphase Efre 3D (FAME)
- Half-fourier rapid acquisition	- Liver Acquisition with Volume Acceleration (LAVA)
- Single-shot fast spin echo	- T1-weighted high resolution isotropic volume examination (THRIVE)
- Single-shot turbo spin echo	- Volumetric Interpolated Breath-hold Examination (VIBE)
- 3D T2-weighted fat-saturated sequence	

Software: Chop-fMRU

To evaluate the obtained MRU images several software options are available. We choose to focus on a program called CHOP-fMRU which was developed in the radiology department of the Childrens Hospital of Philadelphia, USA (23). The programs accepts the images in DICOM (Digital Imaging and Communications in Medicine) format and are then used to place and calculate regions of interest for the program to analyze. These have to be placed on aorta at the approximate level of the renal arteries, as well as on the kidneys in which intensity changes over time are measured. The ROI on the Aorta is used as a temporal frame of

reference used by several measurement units, indicated by the first appearance of contrast agent. Regions of interest also have to be placed on the kidneys, both in anterior-posterior and lateral orientation as well as within the renal parenchyma.

After automatic segmentation performed by the program, the highlighted areas can be reviewed and corrected. This is important not only for verification of accuracy, but also because the program itself does not possess motion correction abilities. With final analysis completed, resulting output is shown in *Table 3*:

Table 3: Results as output by CHOP-fMRU (23) (www.chop-fmru.com)

Parameter	**Description**	**Unit**
Calyceal transit time (CTT)	Time needed for the contrast agent to reach the calyces	min, sec
Renal transit time (RTT)	Time needed for the contrast agent to reach the ureter below the level of the lower pole of the kidney	min, sec
Tim-to-peak (TTP)	Time to reach maximal parenchymal enhancement	min, sec
Whole volume	3-D volume of the renal parenchyma and pelvicalyces	ml
Parenchymal volume	3-D volume of the contrast-enhanced renal parenchyma	ml
Volumetric differential renal function (vDRF)	Split renal function	%
Patlak differential renal function (pDRF)	Split renal function	%
Volumetric and Patlak differential renal function (vpDRF)	Split renal function	%
Difference vDRF and pDRF	Difference between vDRF and pDRF	%
Patlak	Patlak number	ml/min/ml
Body surface area Patlak (BSA Patlak)	Absolute Patlak number corrected according to body surface area	ml/min/ml

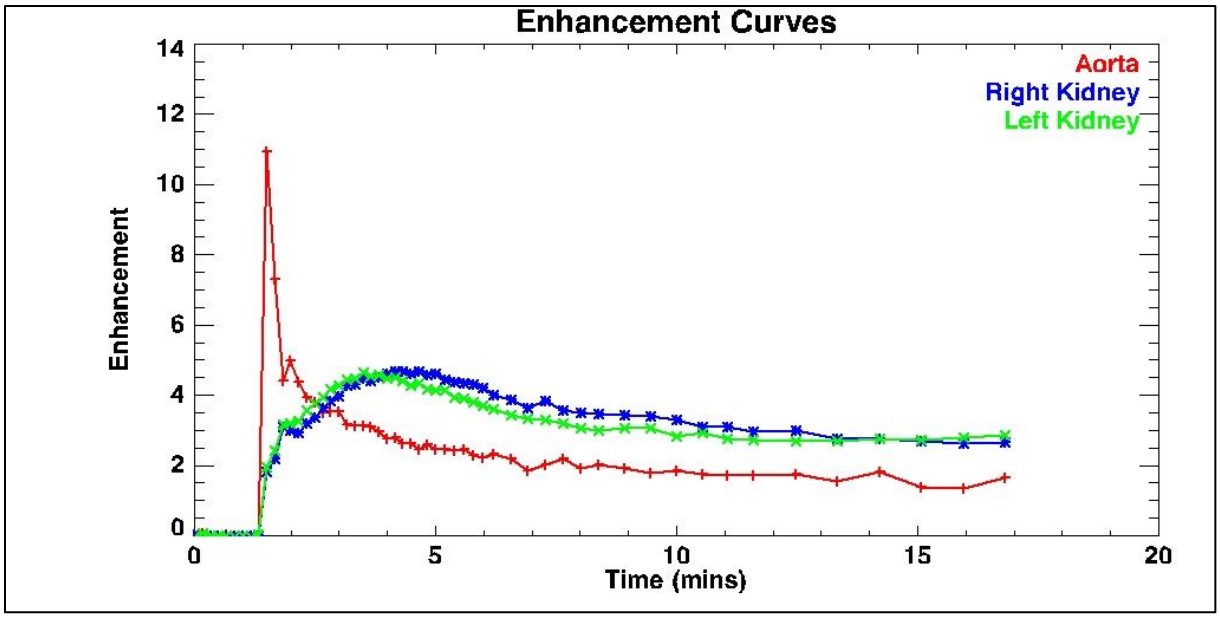

Figure 1. Enhancement Curves as output from CHOP-fMRU showing change in signal intensity over time for regions of interest on aorta and kidney parenchyma.

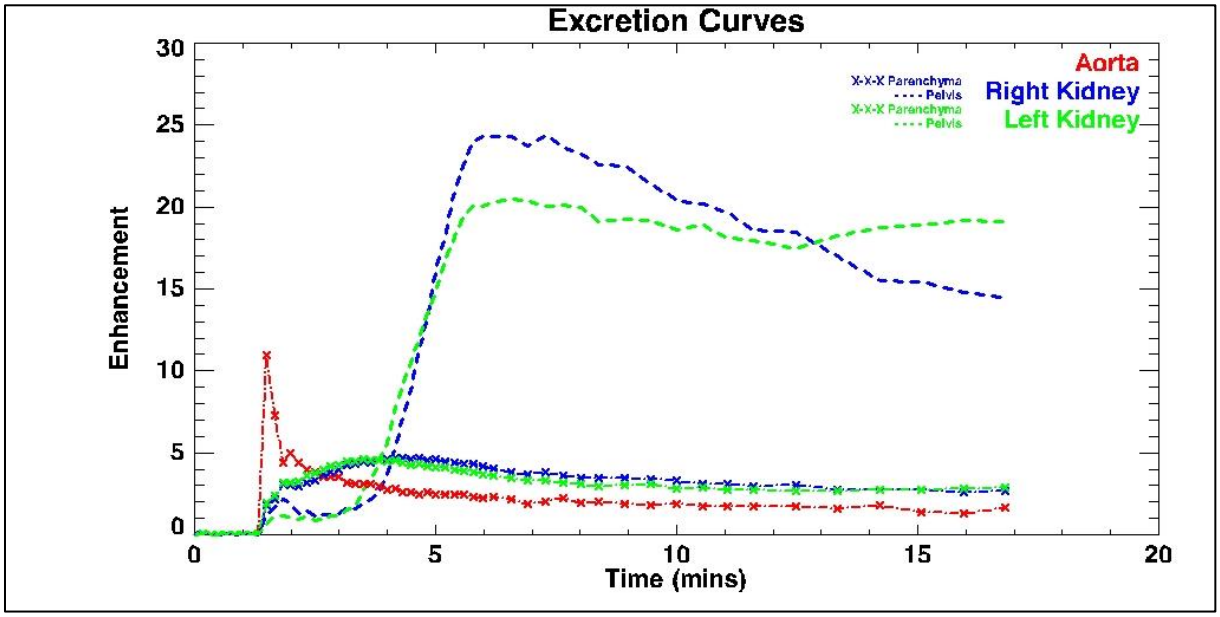

Figure 2. Excretion Curves as output from CHOP-fMRU showing change in signal intensity over time for the aorta and pelvicalyces.

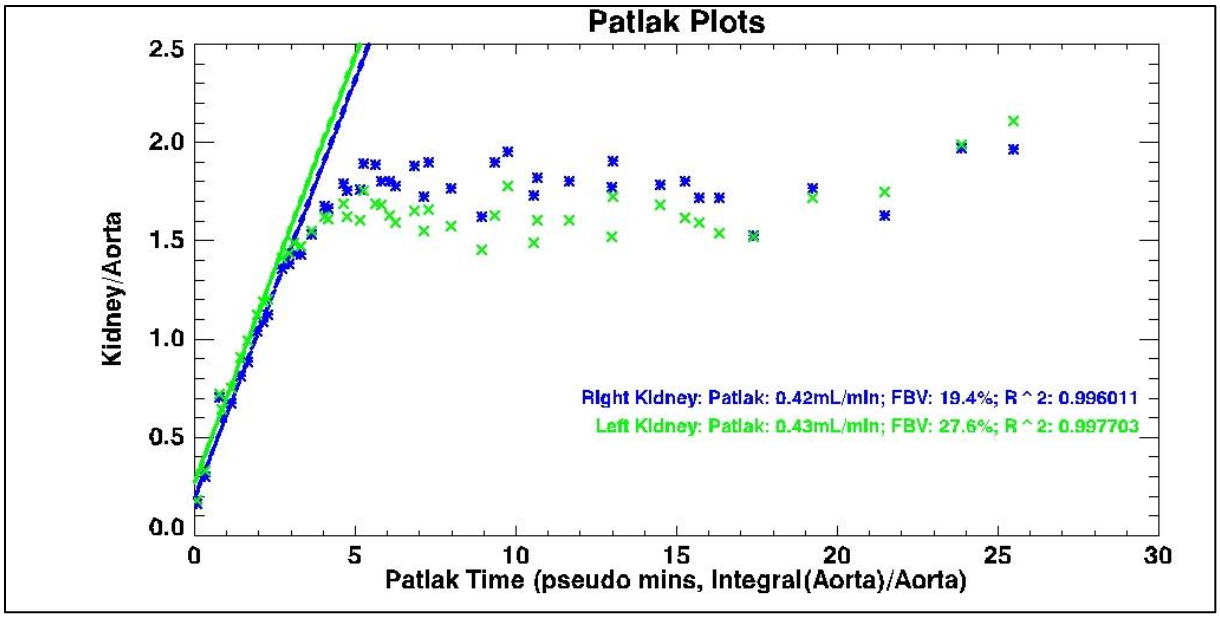

Figure 3. Patlak plots used as indicator for GFR values where:

$$\text{x-axis} = \frac{\int Aorta\ (Enhancement\ curve)}{Aorta\ (Enhancement\ curve}$$

$$\text{y-axis} = \frac{Kidney\ (Enhancement\ curve)}{Aorta(Enhancement\ curve)}$$

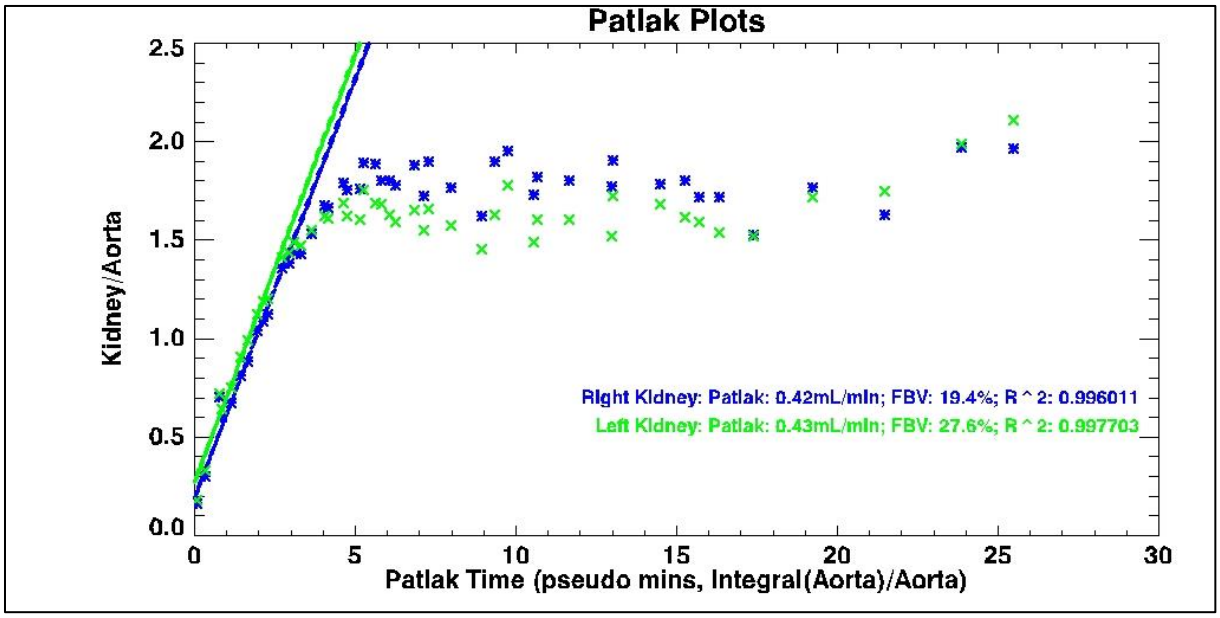

Figure 4. Patlak maps visualizing Patlak numbers over renal area.

1.3 Scope of this dissertation

MR Urography has proven to be able to adequately assess renal anatomy and function without the added risk of radiation exposure (15,29,51,52). Many of the indications previously reserved for CT, nuclear medicine or other procedures involving radiation exposure have seen an addition towards the usage of MR techniques (17,53,54). At the same time this means an adaptation to the prolonged scanning time, where motion artifacts have come to play a more significant role regarding image quality. Methods of minimizing movement artifacts prior to post-processing vary in efficiency. With the exception for nuclear medicine imaging, where the low spatial resolution does not justify or benefit from respiratory gating, breath-hold techniques are a viable option in adult patients with adequate compliance and can be used in sequences completed within a certain timeframe (29). Respiratory gating is used as breathing motion control not only in post gadolinium dynamic imaging, but also in renal DTI (55).In children where the required level of compliance is not obtainable, sedation can prove a viable option (25,53,56). Together with respiratory gating quality images may be obtained but with substantial limitations in temporal resolution.

Post-processing is not able to extract information from an image that does not meet the required level of quality. Distorted anatomy, low resolution pictures or motion artifact can only be improved to some degree, meaning that the selection of the optimal imaging sequence is of great importance (57). Sequences that can be used when holding ones breath will not suffice when used with respiratory gating, which would require faster sequences (29). Working without a static frame of reference which is the case when movement is present in the dataset, reliably mapping world to voxel coordinates becomes difficult.
In this dissertation we try to optimize information gain in MR Urography sequences where the respiratory gating method might be used. The idea is that motion correction is applied in the post-processing stage on a full dataset rather than attempting to limit motion artifacts in a relatively incomplete image series obtained by respiratory gating. Additionally this method of motion correction is not limited to sequences where respiratory gating is utilized, but can help to streamline the workflow in post-processing. This becomes evident when reviewing what additional tasks have to be completed in popular analyzing software like CHOP-fMRU (Children’s Hospital of Philadelphia, Philadelphia, PA, USA) and ImageJ (RSB, Bethesda, Maryland, USA) before image series can be evaluated by a physician. Variations in kidney placement are not an obstacle as the regions of interest still have to be placed manually. If

software were able to recognize the kidneys automatically, including placement of regions of interest over the appropriate structures, valuable time might be saved and thereby reducing the interval between imaging and image evaluation. One step in that direction is motion correction.

2. Goal and hypothesis

Motion artifacts in MR imaging are an ever present concern, leading to decreased image quality and ultimately reduces diagnostic accuracy. In this dissertation we hypothesize that information gain from MR urography imaging can be improved and post-processing optimized by utilizing kidney tracking software in an environment requiring no additional intervention by clinical personnel. By experimental simulation in a software model we hope to confirm that kidney tracking involving kidney identification with subsequent motion correction, followed by automated placement of regions of interest with analysis of time-intensity-curves is feasible. As a proof of principle experiment we want to ascertain if this approach to image analysis optimization is possible and reliable, creating a platform for further research regarding adaptation to real world MR imaging.

3. Material and methods

For this experiment we generate monochromatic image series for 100 kidneys where we simulate kidney movement. This is done in an automated script in Matlab (TheMathworks, Natick, NA, USA) by shifting the kidney in each image vertically using a sinusoidal function, over a timeframe of 60 images. Additionally, application of contrast agent is simulated in kidney compartments of cortex, medulla and renal pelvis, shown as intensity change over time.
Having generated image series representing MRU scans that do not utilize motion correction, we try to negate the kidney motion using kidney tracking on half of the simulated patients, thus retrieving a new dataset containing images with stationary kidneys. This enables automatic assignment of regions of interest in the next step, so that contrast flow and concentration change can be measured in each compartment. Finally the retrieved output intensity curves are compared to the original input curves to ascertain with which level of accuracy the measurement was performed.

The investigation was carried out in a software model utilizing Matlab from Mathworks (Natick, NA, USA). There were several advantages to this approach. Firstly the respective candidates with functional kidney scans would have to be found in a database. This search for eligible patients with similar imaging protocols and parameters would have taken a considerable time while using real fMRU images would have required a much more complex software, as more details would have to be analyzed. In these early stages, a less complicated experiment allowed for faster evaluation and completion of each task while maintaining a representation of real world circumstances needed for a proof of principle experiment.

Secondly an important obstacle to overcome concerns the matter of application of contrast agent. Even though the relevant Gadolinium-DTPA has few side-effects, predominantly found in patients with contraindications to the examination itself, the correct application is crucial in regards of getting images that qualify for evaluation (16). Using a software model, an arbitrary number of patients can be simulated, including the necessary breathing motion and application of contrast agent.

As this is a proof of principle experiment, the aim is to verify if an automated form of fMRU imaging could become a feasible method for evaluating renal function and anomalies. This represents a step in the direction of creating viable methods for automatic recognition and analysis of moving structures in clinical imaging. The first step in this project is the generation of patient data that adequately simulates fMRU imaging.

3.1 Simulation

3.1.1 Generation of image series

Image generation was undertaken in the Matlab 2010 (7.11.0.584 R2010b), where the original images of the moving kidney were created. For every simulated patient a series of 60 images were generated, comprising of a grayscale background together with the moving kidney, shown from a coronal view and calix orientation to the right. A template matrix with dimensions 240x120 pixels (p) was used as a canvas. For the purpose of simulating MRI imaging, grayscale was chosen as palette.

In the main function the kidneys are placed on the canvas, changing position for every new image generated. In this function the anatomic substructures are defined, combined with the change in brightness intensity, visualizing the perfusion of the contrast agent of respective compartment: cortex, medullae and calyx. The position was randomized for each patient around a static central point on the canvas, with both vertical and horizontal variance. Following the creation of the kidney, a layer of white noise with uniform distribution is added to more accurately portray the signal-to-noise ratio of an MRI-machine. Finally the image is stored in BMP file format.

3.1.2 Anatomic structures

The kidney in this simulation is a simplified version of its anatomical origin, but still holds the relevant structures needed for kidney function evaluation. It is comprised of three compartments: the cortex, three medullae and the calix. The cortex represents the parenchyma, encapsulating three pyramid shaped medullas lying on the left side of the kidney pointing to the right, together with the calyx, oriented to the right side. These structures need

the parameters for positioning, size in radius and arc opening, together with the gamma value that represents the intensity in brightness for all compartments.

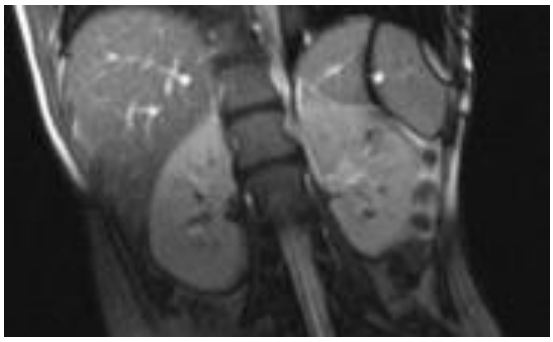

Figure 5. Anatomical structure MRI.

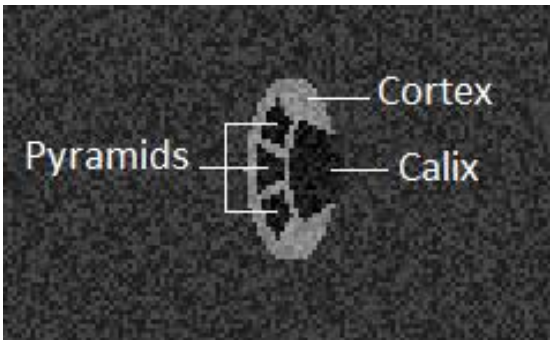

Figure 6. Anatomical structure program.

Creating the shape of the kidney, represented by the cortex, is done using an ellipsoid function, the output of which is a 3D elliptical object, scaled to a 2D canvas. The medullas and calix are generated using circle radius and positioning, combined with arc length to output a pyramid shaped object. Dimension for the cortex is 20x40p, medullae radius 7-8p with arc openings of 50 degrees, and calix radius of 5.5p with arc opening of 135 degrees.
Positioning of the anatomic structures is done relative to the kidney central coordinate c. Even though the central point of calix and medullae may be out of bounds in regard of the ellipse, defining the arc opening and radius will place them inside of the kidney region. Thus the calix is positioned at $x = c + 15$, $y = c$; medullae at $x = c + 10$ and $y = c$ $(-5, 0, +5)$.

3.1.3 Simulation of vertical breathing motion

To simulate a breathing motion, as is present in fMRU imaging, a sinusoidal function was used, allowing for an oscillation with a vertical amplitude of 30p around the center position. The kidney in each image is thus vertically shifted by formula: $y = 30 * \sin(n)$ n ranging from 1 to 60. In each patients image series a central fixed point is chosen with a horizontal variance of 10p and a vertical variance of 20p, remaining the same for the duration of the simulation. Purpose of which is to indicate the differences in patient anatomy, with varying kidney location and breathing motion.

Regular datasets from fMRU imaging are done by scanning defined areas that are triggered when the patient is exhaling. Creating the continuous image series in this project enables the theoretical collection of greater data volumes, giving the physician greater precision in diagnostics and consequently selection of optimal therapy. Considering that fMRU is a popular choice in pediatrics where movement cannot always be suppressed, and the level of compliance may not be high enough, being able to counteract these movements would be beneficial.

Being an exaggeration of extreme movement, vertical shifting of this magnitude is seldom found in reality. But for purposes of testing the movement stabilization capabilities of the program, this decision was deemed relevant.

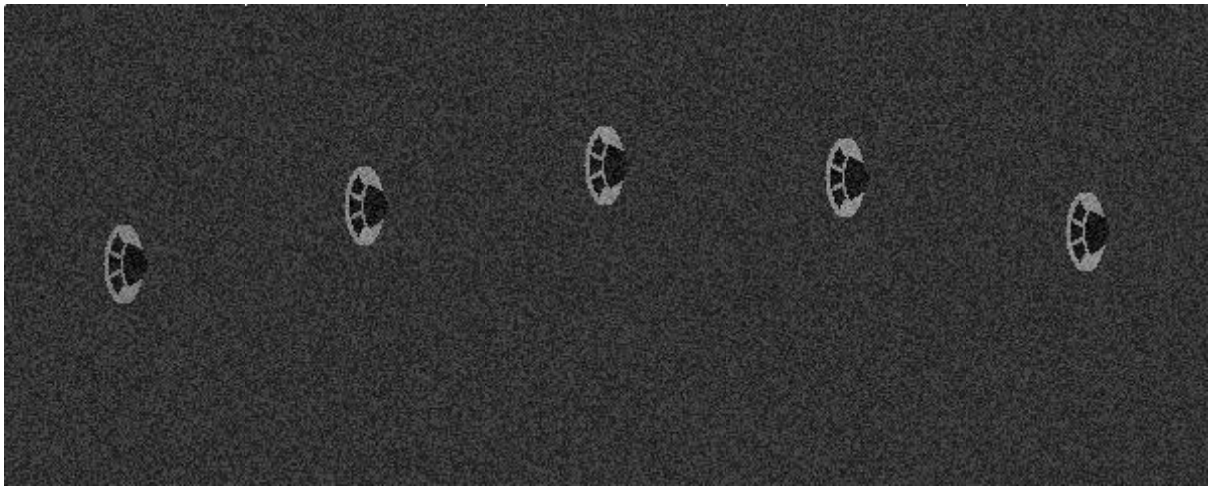

Figure 7. Simulated breathing motion where set time interval between frames equals 10 seconds.

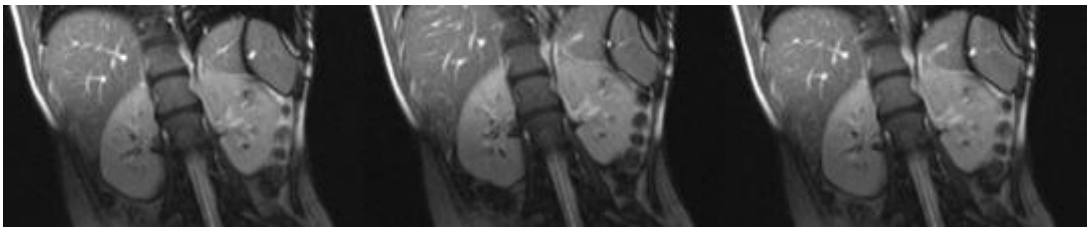

Figure 8. Breathing motion in MRI, variable states of exhalation.

3.1.4 Contrast agent curve

To simulate the change in intensity of the contrast agent over time, gamma curves were created for each of the three compartments using Toolbox SPM5 (FIL, ION, UCL, London). This Toolbox contains a function which produces a hemodynamic response curve, mirroring

physiological reactions of blood flow (58). These values range from 0 to 1, value 0 representing black (no signal), value 1 representing white (maximum signal). The curves range from a baseline of 0.1, reaching maximum values of 0.55 (cortex), 0.7 (medullae) and 0.88 (calix).

A linear relationship between brightness intensity and contrast agent concentration is assumed, which would enable direct interpretation of plotted data without further calculations (23).

The timeframe of the fMRU can vary depending on scanner model, previous acquisition times lie in the 8.4 – 9.7 s interval per dynamic volume (23). Those resulting images are dependent on the patient's exhalation, which is when a new image is taken (59). As the program uses a continuous measuring method, this factor can be ignored. Still for simplicity sake in this project the acquisition time for each frame is set to 10 s. As each patient's image series amounts to 60 images, this equals a temporal resolution of 10 m for a complete fMRU testing cycle.

The onset of contrast agent perfusion varies for each compartment. Mimicking reality the first compartment to be affected of this is the cortex (t = 8), followed by the medullae (t = 20) and culminating in the calyx (t = 40) from where it drains into the ureter. Contrary to real life MR urography images where contrast agent would first appear heterogeneously in the kidney calyceal system, in our experiment contrast agent flow is homogeneously portrayed in each compartment. Also, the declines in the later part of the intensity curves as they would have been in real life are not depicted, as this was not corrected for when generating the gamma curves in the toolbox SPM5.

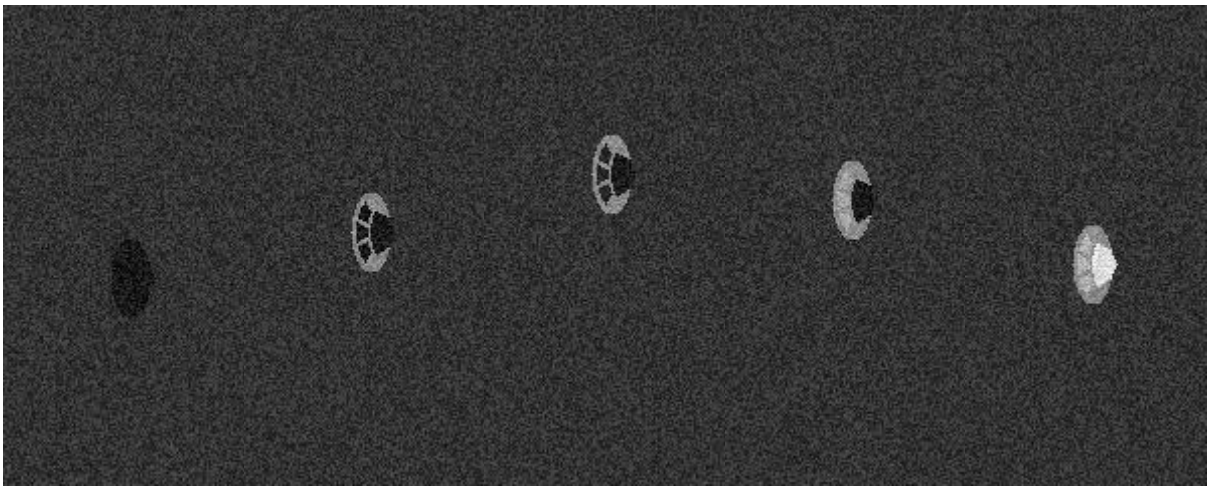

Figure 9. Kidney series with breathing motion and perfusion.

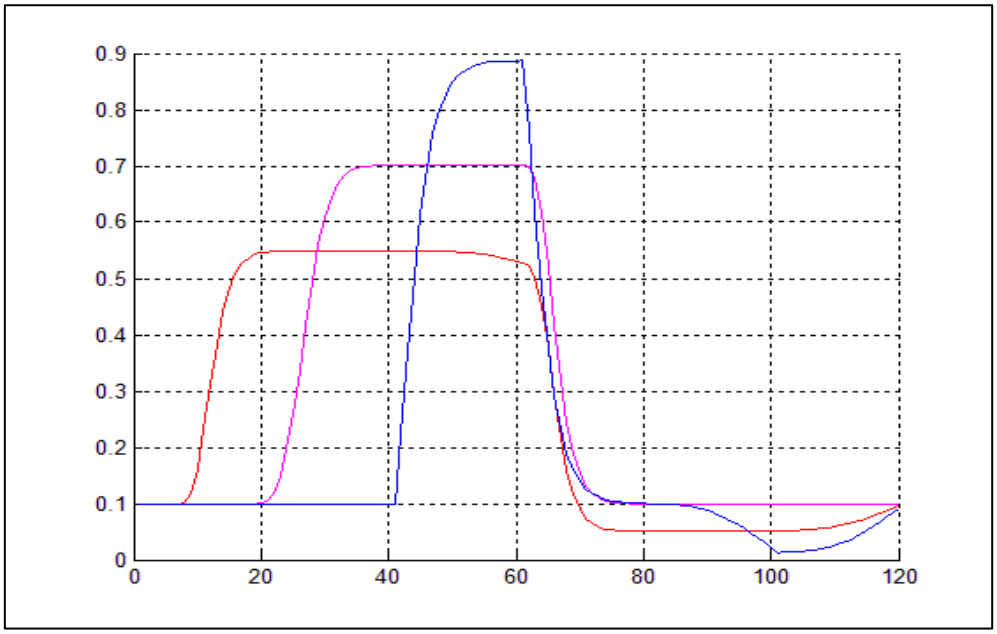

Figure 10. Input gamma curves. Cortex = red, Medullae = magenta Calyx = blue.

3.1.5 Adding noise

A layer of uniformly distributed noise was added to the images, to better portray the signal-to-noise ratio present in MRI images. This was done creating a randomized matrix with the same dimensions as the original image. The randomized values ranged from -0.1 to 0.1, resulting in a uniform noise range of 0.2. This requires the gamma curves minimum and maximum values to be shifted by +0.1 from the baseline of zero, respectively -0.1 from the maximum of one. Not meeting this requirement would cause part of the noise being lost below 0 or above 1,

resulting in a distorted mean value when analyzing the images. In order for the intensity change to be measureable, the gamma curves have to be inside an interval between 0.1 and 0.9. Both matrixes are then added to each other to create the final image.

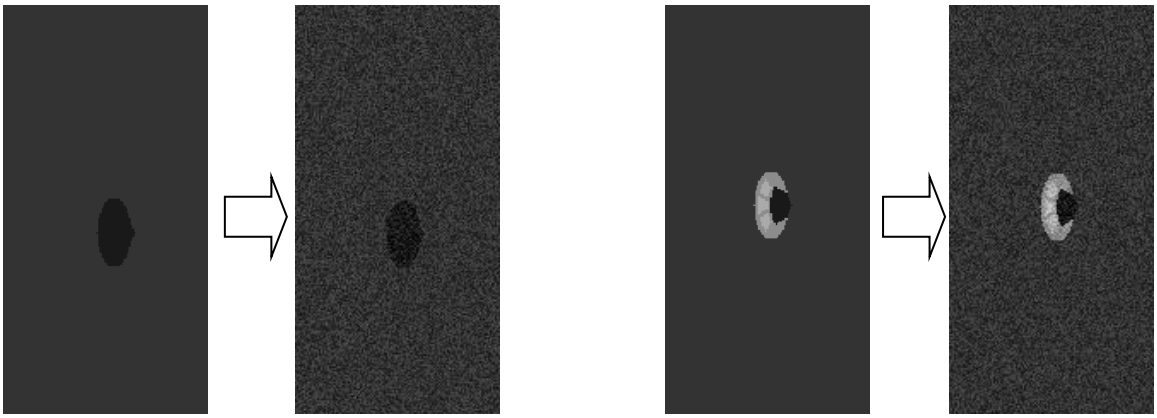

*Figure 11.*Before and after application of noise layer.

3.2 Analysis of data

3.2.1 Stabilization of vertical breathing motion

Stabilizing the moving kidney is done by sequentially running two scripts that result in two new sets of images, the cropped stable kidney and its equivalent binary images. First a series of image enhancements are done to contrast and find the kidney on the canvas, including smoothing with median and Wiener filtering (60), creating grayscale observation windows with thresholding, and lastly converting resulting images into binary. Following identification of the kidney position in each image, the relevant area is cropped based on its extreme values for horizontal x and vertical y values, resulting in a new series of images containing the now static kidney. These scripts are run prior to visualized simulation and actual measurements, combining several advantages. The intermediate evaluation of the program is made easier, as faulty conversions and cropping can be quickly identified. More importantly, the actual measurements are much more efficient as the images don't have to be converted in real time, giving a quick and smooth analysis. In real life this would equal background processing of images, ideally being ready for interpretation when the physician requests them from respective databases. Resulting images have dimensions of 32-33x50p.

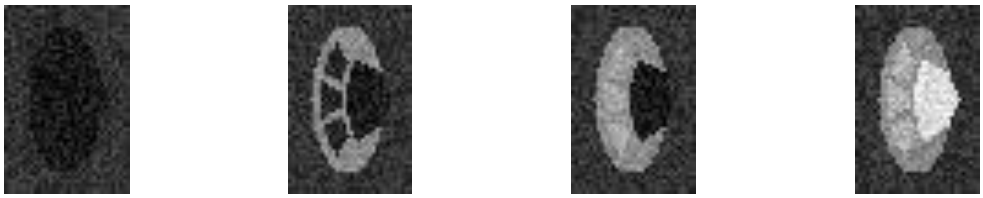

*Figure 12.*Kidneys cropped from original image.

3.2.2 Automatic analysis of image series

Being a series of images with the object changing position and brightness intensity over time, finding an anchor from where to orient is important. Compartments that start out as darker than the background, like the cortex, will eventually turn brighter as the contrast agent is simulated. The need to identify the breaking point where simulated kidney goes from dark to bright arises, as from that point on some of the filtering effects have to be reversed or omitted entirely in order for the program to recognize the kidney shape.

In Matlab an object in a binary image is identified as pixels with value 1, remaining pixels values being 0. The kidney in the images before the breaking point is darker than the background, which can be solved by inverting the binary image, resulting in a bright kidney shape. Consequentially, the images after the breaking point don't have to be inverted, as the contrast agent simulates an increase in brightness, giving the kidney a hyperintense signal relative to the background, thus making the program recognize the kidney shape.

pre-bp pre-bp bp post-bp

*Figure 13.*Binary kidney masks. Bp = breaking point.

Having stabilized the breathing motion of the kidney and converting the images into binary yields masks of different size and shape. The following task becomes finding the biggest mask in the binary series from which the minimum and maximum values for the vertical and horizontal edges can be measured, as well as the kidney center. These coordinates are used as point of origin for placement of the regions of interest, which make out the windowed region

where the actual measuring of brightness intensity takes place.

3.2.3 Regions of interest

In order for the program to measure the changes of intensity over time, the regions of interest had to be defined, making it possible to analyze the curve for each compartment independently. After stabilizing the images from the breathing motion, defining the measurement windows can be done regardless of vertical motion, resulting in static regions of interest. The geometry of the windows is predefined, based on the shape of the kidney created for this project. Previous functions return the coordinates for the vertical and horizontal edges, which are then used by the Mask-functions to create the ROI-Masks and display the results in respective data plot window.

In total, four ROI-windows were created: one for the medullae, two for the cortex and one for the calix. It is assumed that one of the medullae has its center point in the middle of the kidney. Similarly the two windows for the cortex are placed at its vertical poles, leaving the calix-window for the right sided center position. The images are in 8-bit BMP format that holds support for up to 256 colors (61) The program scans the defined regions of interest and calculates mean values for each window. A mean value is also calculated for the two cortex windows that together generate a higher amount of data, giving higher precision to the measurement. These values are then scaled to an interval between 0 and 1 to allow for a more efficient overview when evaluating the output curves.

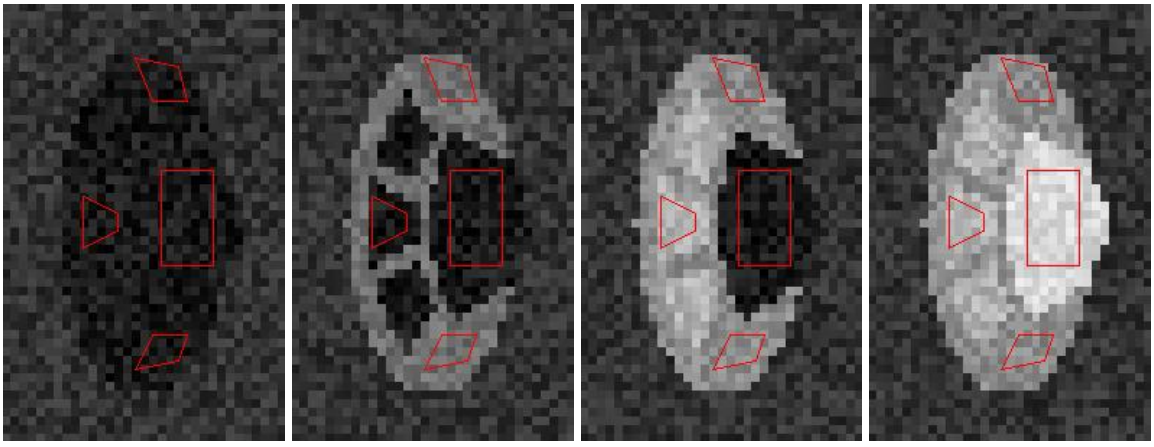

Figure 14. Regions of interest.

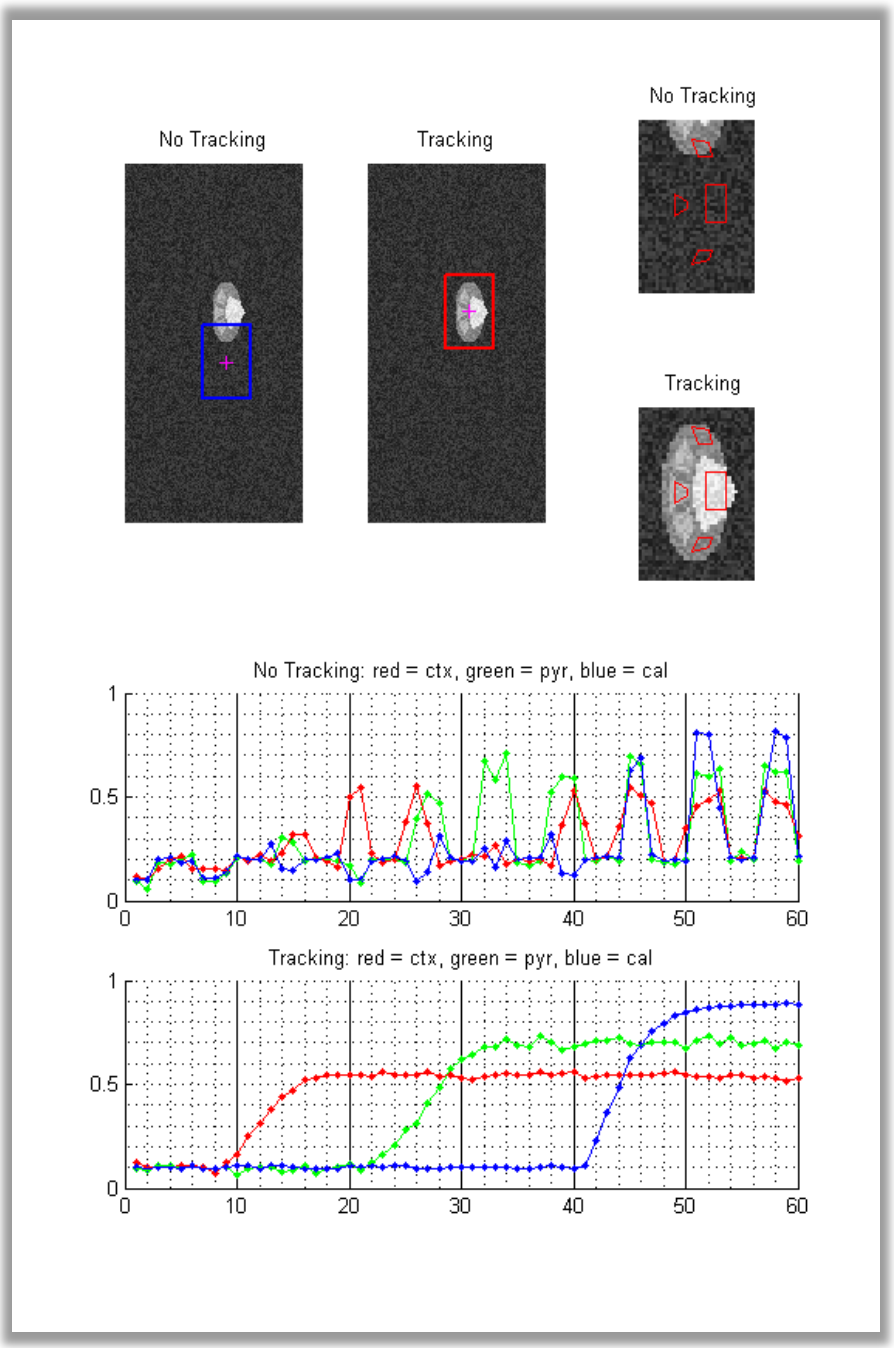

*Figure 15.*Graphical user interface of Simulation.

3.2.4 Statistical methods

Data is acquired through measurements in the ROI-windows which outputs the mean intensity values of all pixels. These range from zero to 255 as defined in the 8-bit BMP format (61). Being able to compare this data to the original gamma curves requires a scaling to an interval between zero and one. The data is stored in variables for each compartment connected to each

patient. Further calculations are carried out by subtracting the ROI-data from the gamma-curves, resulting in a plotted graph with an expected median of zero.

3.2.4.1 Wilcoxon signed rank test

The data is analyzed with the Wilcoxon signed rank test (11) for zero median. This method is a built in function in Matlab and performs a two-sided signed rank test with the assumption that the data comes from a distribution with a median of zero. The reason for choosing this method is because it is a non-parametric hypothesis test, which can be used when evaluating two matched samples, in this case the gamma-curves and the actually measured intensity curves.

Using the Wilcoxon signed rank test on the resulting data outputs several variables which can be used in the statistical evaluation. These comprise of the results of the hypothesis test, p-value and three additional variables, including sum-difference, z-value and the Wilcoxon signed rank. Sum difference is the cumulative area under or over the curve in relation to the zero base line. In effect every value that differs from zero is added together to indicate quantity difference. Z-Value or standard score is the measurement of standard deviations. A positive value indicates that the number of standard deviations is above mean, a negative value that they are below the mean. The outcome of the hypothesis test can be either $H = 0$, indicating that the null hypothesis cannot be rejected, or $H = 1$, indicating that the null hypothesis can be rejected, all at the 5% significance level. In this case the desired results are $H = 0$, meaning that the hypothesis "median is zero" cannot be rejected. Ideally this would be combined with a p-value above 0.05, stating the likelihood of observing the same test results explained by random chance.

3.2.4.2 Bonferroni correction

As a part of the statistical evaluation of this project, the occurrence of multiple testing has to be taken into consideration. The problem of multiplicity describes a statistical phenomenon where the chance of a test being statistically significant just by chance increases with the number of tests. (63) Finding out if this correction is sensible and valid can be done by

calculating the probability of getting at least one significant test result just by chance. The formula for this is defined as

$$\alpha = 1 - (1 - \alpha)k$$

where $\alpha = 0.05$ (5% significance level) and $k = 150$ (number of tests). With the values in place the probability for obtaining at least one significant test result by chance becomes 0.9995(4444502), practically guaranteeing said outcome. With the Bonferroni correction, this can be taken into account and may result in that the required significance level alpha of 5% might be lower when repeating the Wilcoxon signed rank test multiple times. The new formula for alpha is thus defined as

$$\alpha = \acute{\alpha}/\sqrt{n}$$

With $\acute{\alpha} = 0.05$ and $n = 150$, the resulting α equals 0.0041 and is used in comparison to the p-value.

4. Results

4.1 Tracking group

4.1.1 Input curves

Graphs of the gamma function for each compartment (cortex, pyramids and calix) simulating the perfusion of contrast agent over time. Values range from 0.1 to 0.9 where 0 indicates no perfusion and 1 shows maximum possible perfusion. In the simulation this is shown as an increase in brightness with zero being black and one representing white. The Y-Axis units are the measured brightness from zero to one, and the X-Axis shows the number of frames from one to 60, equaling the temporal resolution.

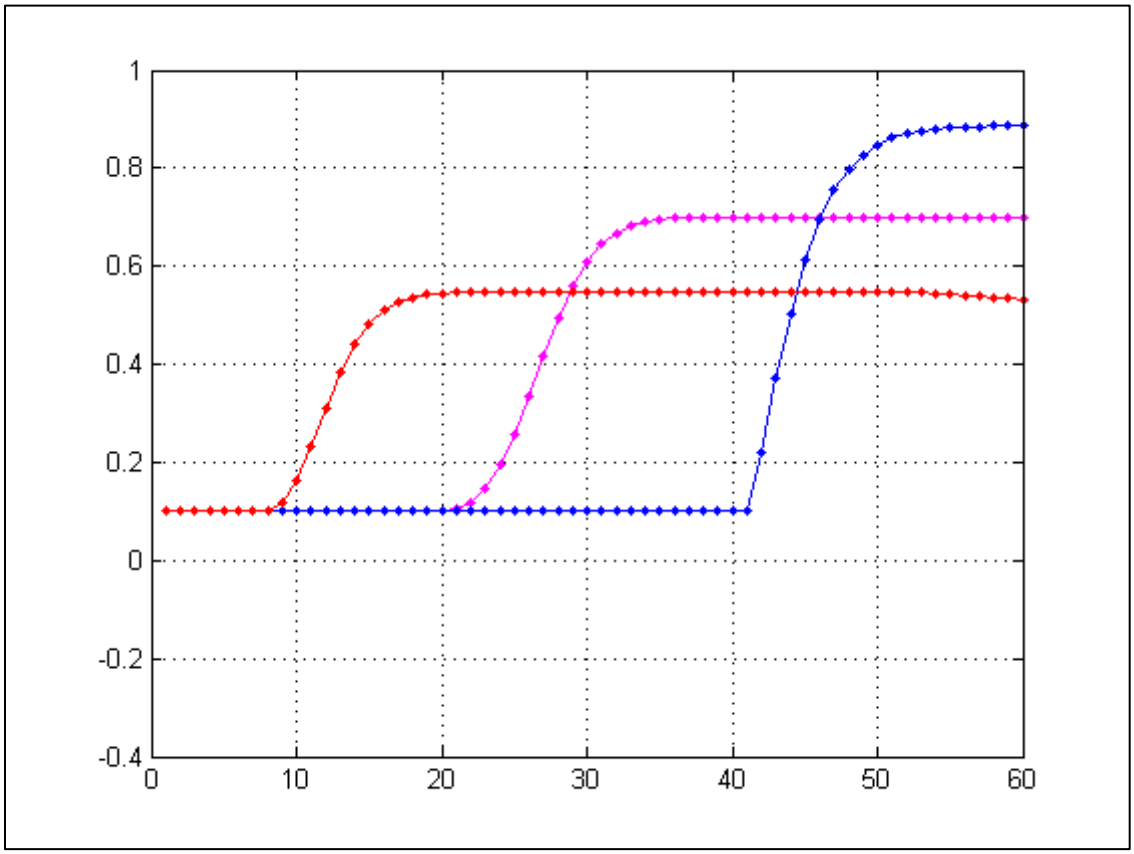

Figure 16. Input gamma curve for cortex (red) pyramids (magenta) and calix (blue).

4.1.2 Output Curves

Graphs of the measured brightness intensity for each compartment (cortex, pyramids and calix). Values range from XX to XX where 0 indicates no perfusion (black) and 1 shows maximum possible perfusion (white).

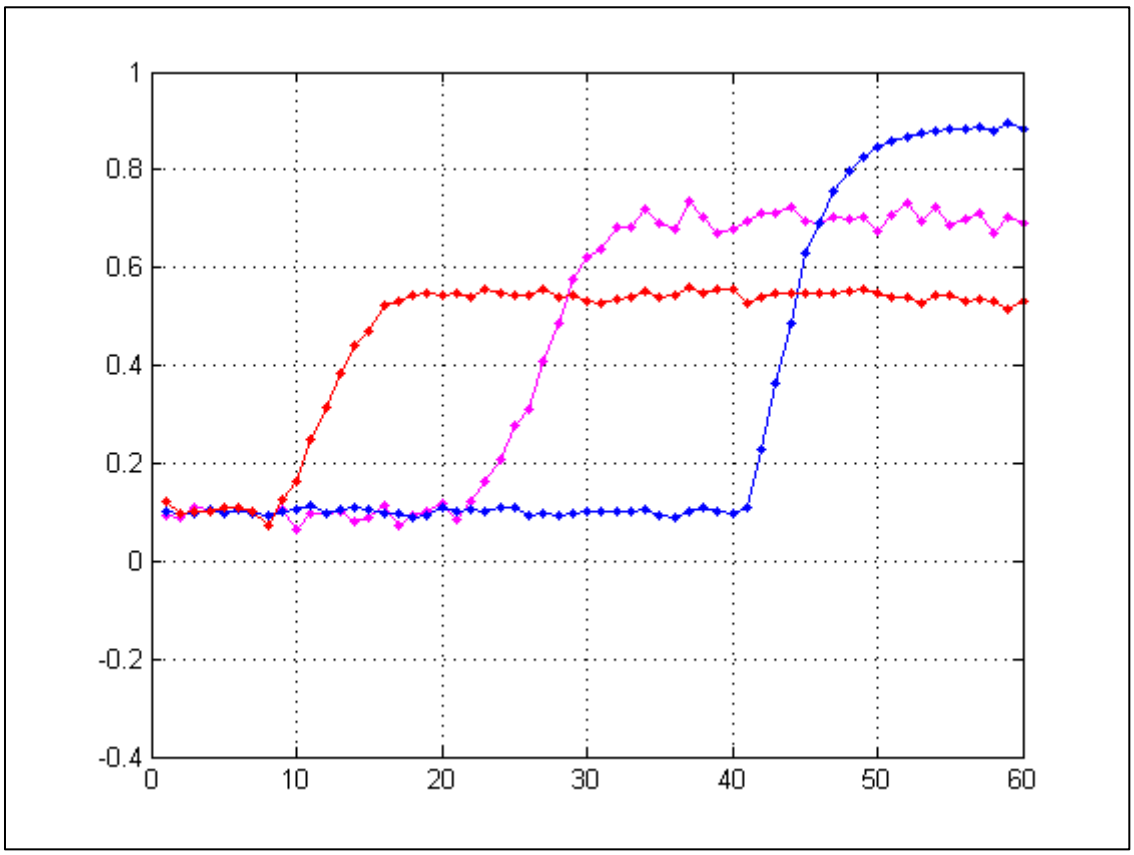

Figure 17. Results curves for Cortex (red), Pyramids (magenta) and Calix (blue).

4.1.3 Comparison of curves

Comparing the data of the curves is done by subtracting the output data from the input data, ideally yielding a graph with a baseline of zero. This would mean that the program is able to detect the right anatomic structures of the kidney, and at the same time measure the intensity change in said compartment in accordance with the originally defined gamma curves. The addition of noise should create a certain amount of variation that can be observed in the comparison curves.

The negative spikes indicate that too much was subtracted from the input gamma curve, and

the positive spikes indicate that there was not enough subtracted. The Y-Axis units are the measured brightness from zero to one, and the X-Axis shows the number of frames from one to 60, equaling the temporal resolution.

4.1.3.1 Cortex

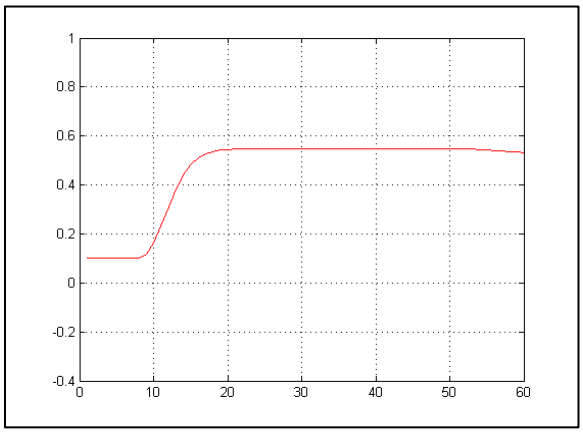

Figure18. Gamma function curve.

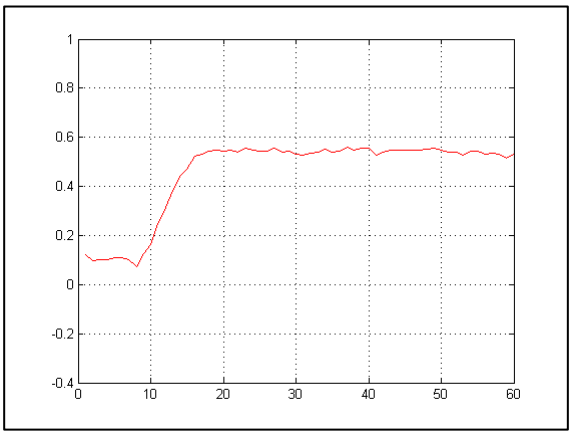

Figure 19. Output curve.

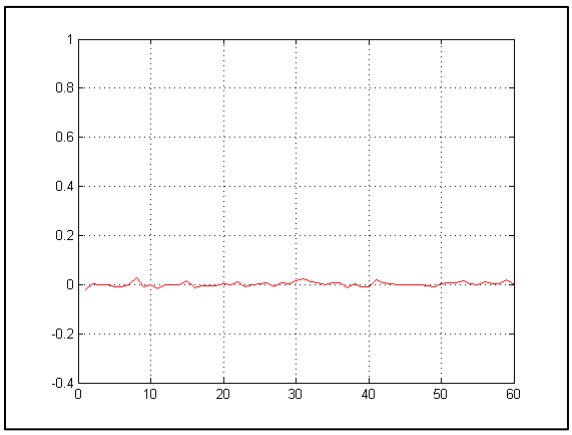

Figure 20. Results comparison curve.

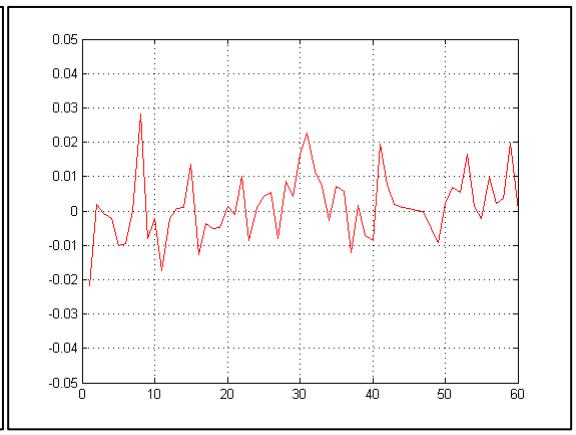

Figure 21. Magnified comparison curve.

4.1.3.2 Pyramids

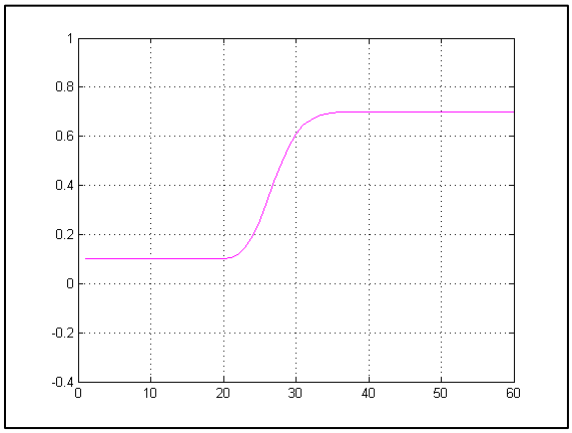

Figure 22. Gamma function curve.

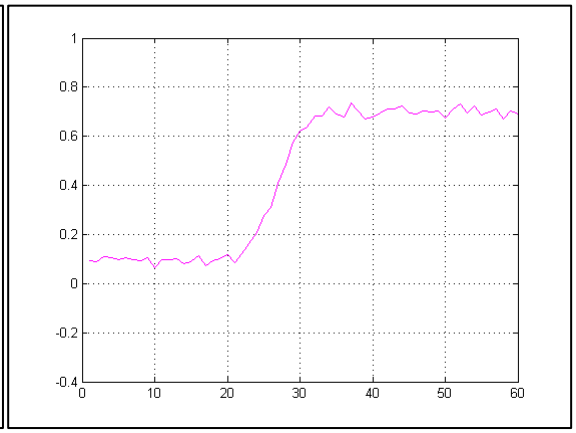

Figure 23. Output curve.

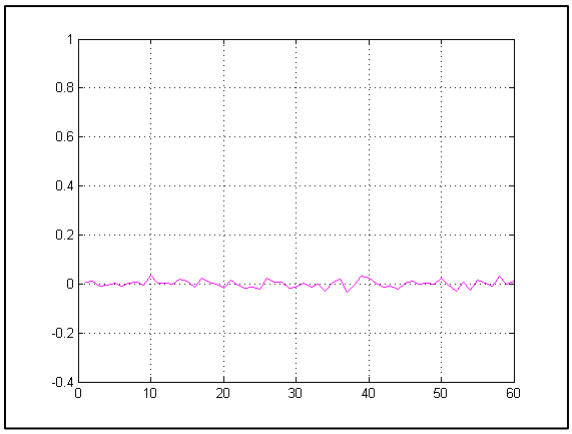

Figure 24. Results comparison curve.

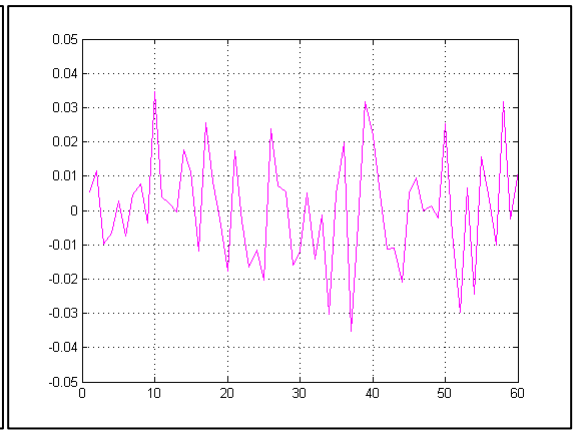

Figure25. Magnified comparison curve.

4.1.3.3 Calix

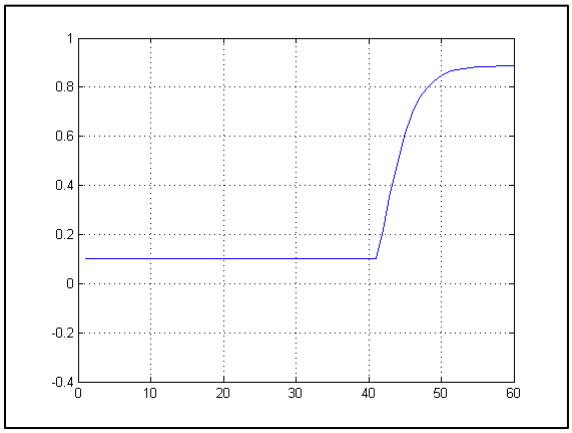

Figure26. Gamma function curve.

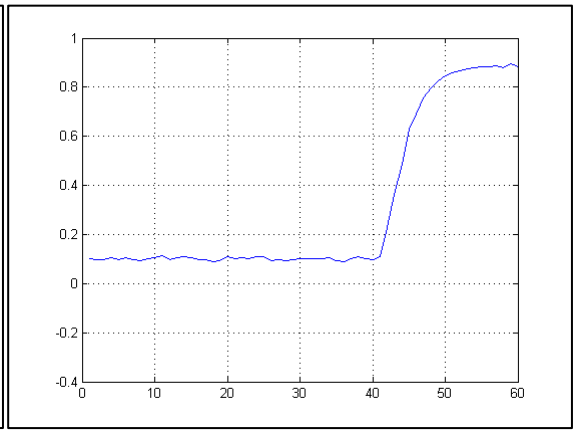

Figure 27. Output curve.

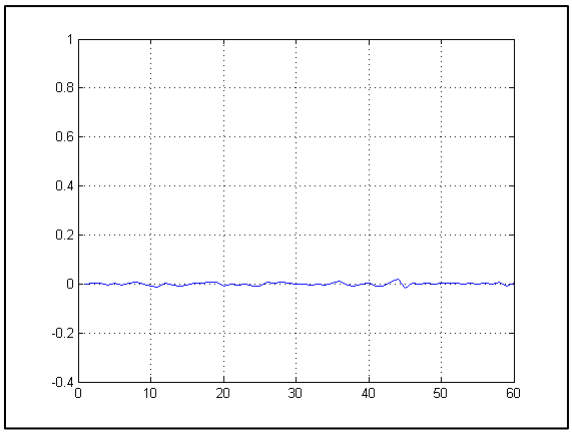

Figure 28. Results comparison curve.

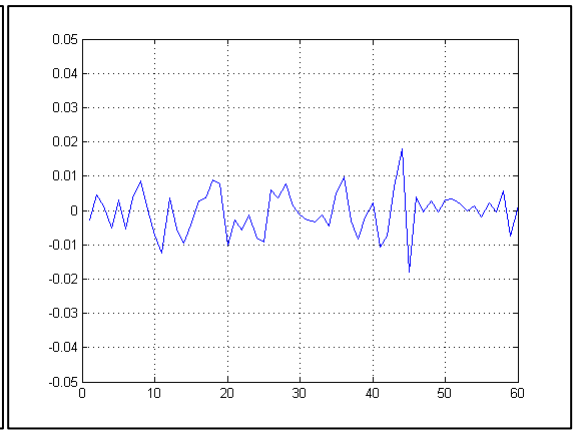

Figure 29. Magnified comparison curve.

4.2 Statistical analysis

4.2.1 Wilcoxon signed rank test

In table 4 the results and output of the wilcoxon signed rank test function are found, as well as new alpha value corrected with bonferoni formula. For each patient and compartment the statistical results are calculated and compiled consisting of:

- Sum-Difference: accumulated difference relative to baseline of zero
- Z: (Z-value) shows number of standard deviations above (positive value) or below (negative value) mean
- WSR: Wilcoxon signed rank
- p: probability value (p-value) ranging from 0 to 1
- H: Hypothesis test can be true or false

4.2.2 Bonferroni correction

Based on the 5% significance level alpha, when correcting for multiple testing the new alpha equals 0.0041. The last column in Table 4 shows that all p-values meet the criteria of being greater than alpha. Consequently the hypothesis tests become false and the H0-Hypothesis can not be rejected. Therefore it can be assumed that the test is accurate in its assumption of having a median of zero.

4.2.3 Results table for tracking group

Table 4. Statistical output of kidney tracking measurements.

Pat	structure	S-Diff	Z	WSR	p	H	p > 0.0041
1	pyr	0,042659	-0,47115	851	0,637534	FALSE	1
1	ctx	0,086799	-1,0159	777	0,309676	FALSE	1
1	cal	0,029526	-0,4417	855	0,658707	FALSE	1
2	pyr	0,154259	-1,57539	701	0,115167	FALSE	1
2	ctx	0,085054	-0,89812	793	0,369124	FALSE	1
2	cal	0,090379	-1,16314	757	0,244774	FALSE	1
3	pyr	0,047141	-0,35336	867	0,72382	FALSE	1
3	ctx	0,059147	-0,72144	817	0,470641	FALSE	1

Pat	structure	S-Diff	Z	WSR	p	H	p > 0.0041
3	cal	0,054957	-1,15108	732,5	0,2497	FALSE	1
4	pyr	0,100478	-0,72144	817	0,470638	FALSE	1
4	ctx	0,015069	-0,25029	881	0,80236	FALSE	1
4	cal	0,006718	-0,08834	903	0,929605	FALSE	1
5	pyr	0,140254	-0,89076	794	0,37306	FALSE	1
5	ctx	0,003556	-0,22821	884	0,819483	FALSE	1
5	cal	0,027744	-0,05889	907	0,953037	FALSE	1
6	pyr	0,040419	-0,50795	846	0,611487	FALSE	1
6	ctx	0,10887	-1,69317	685	0,090423	FALSE	1
6	cal	0,051935	-1,02697	775,5	0,304432	FALSE	1
7	pyr	0,11857	-0,80978	805	0,418069	FALSE	1
7	ctx	0,039912	-0,14723	895	0,882949	FALSE	1
7	cal	0,092034	-1,75946	676	0,0785	FALSE	1
8	pyr	0,170786	-1,62324	694,5	0,104538	FALSE	1
8	ctx	0,08886	-1,11896	763	0,263156	FALSE	1
8	cal	0,022583	-0,05153	908	0,958901	FALSE	1
9	pyr	0,039018	-0,06994	905,5	0,944245	FALSE	1
9	ctx	0,053724	-0,68463	822	0,493578	FALSE	1
9	cal	0,004452	-0,21717	885,5	0,828074	FALSE	1
10	pyr	0,198402	-1,40241	724,5	0,160793	FALSE	1
10	ctx	0,059571	-0,66254	825	0,507622	FALSE	1
10	cal	0,020919	-0,18404	890	0,853981	FALSE	1
11	pyr	0,038738	-0,39016	862	0,696415	FALSE	1
11	ctx	0,137772	-1,56066	703	0,118604	FALSE	1
11	cal	0,121751	-1,97294	647	0,048503	TRUE	1
12	pyr	0,110166	-0,9202	790	0,357466	FALSE	1
12	ctx	0,110537	-1,66372	689	0,096168	FALSE	1
12	cal	0,117821	-2,0318	639	0,042174	TRUE	1
13	pyr	0,075993	-0,45288	825	0,650636	FALSE	1
13	ctx	0,007419	-0,25029	881	0,80236	FALSE	1
13	cal	0,092458	-1,34355	707	0,179094	FALSE	1
14	pyr	0,13213	-1,08584	767,5	0,277548	FALSE	1
14	ctx	0,016355	-0,44906	854	0,65339	FALSE	1
14	cal	0,000658	-0,12515	898	0,900407	FALSE	1
15	pyr	0,158066	-1,57753	676	0,114674	FALSE	1
15	ctx	0,172721	-2,20848	615	0,027211	TRUE	1
15	cal	0,020138	-0,4076	831	0,683568	FALSE	1
16	pyr	0,01885	-0,28682	847	0,774247	FALSE	1
16	ctx	0,024313	-0,05889	907	0,953037	FALSE	1
16	cal	0,041945	-1,01144	751	0,311806	FALSE	1
17	pyr	0,009721	-0,22821	884	0,819483	FALSE	1
17	ctx	0,072929	-0,94229	787	0,346047	FALSE	1
17	cal	0,024781	-0,51327	817	0,607764	FALSE	1
18	pyr	0,172071	-1,3058	712	0,191619	FALSE	1

Pat	structure	S-Diff	Z	WSR	p	H	p > 0.0041
18	ctx	0,072858	-0,45642	853	0,648088	FALSE	1
18	cal	0,10469	-1,7889	672	0,073631	FALSE	1
19	pyr	0,177673	-1,72998	680	0,083633	FALSE	1
19	ctx	0,143381	-1,88457	659	0,059488	FALSE	1
19	cal	0,037904	-0,64782	827	0,517101	FALSE	1
20	pyr	0,00552	-0,0773	904,5	0,938387	FALSE	1
20	ctx	0,099727	-1,22203	749	0,221698	FALSE	1
20	cal	0,057461	-1,53859	706	0,123906	FALSE	1
21	pyr	0,151738	-0,97174	783	0,331181	FALSE	1
21	ctx	0,112677	-1,42079	722	0,155378	FALSE	1
21	cal	0,071127	-0,84659	800	0,397225	FALSE	1
22	pyr	0,084956	-0,36072	866	0,718309	FALSE	1
22	ctx	0,054701	-0,57421	837	0,565829	FALSE	1
22	cal	0,010453	-0,05153	908	0,958902	FALSE	1
23	pyr	0,022491	-0,19876	888	0,842448	FALSE	1
23	ctx	0,003153	-0,44906	854	0,65339	FALSE	1
23	cal	0,05045	-0,84659	800	0,397225	FALSE	1
24	pyr	0,109326	-0,60384	805	0,54595	FALSE	1
24	ctx	0,05965	-0,75825	812	0,448304	FALSE	1
24	cal	0,004927	-0,6465	772	0,517957	FALSE	1
25	pyr	0,046976	-0,37544	864	0,707332	FALSE	1
25	ctx	0,030252	-0,41225	859	0,680156	FALSE	1
25	cal	0,001906	-0,47115	851	0,637537	FALSE	1
26	pyr	0,014764	-0,22085	885	0,82521	FALSE	1
26	ctx	0,008188	-0,43433	856	0,664045	FALSE	1
26	cal	0,01884	-0,36072	866	0,718309	FALSE	1
27	pyr	0,025408	-0,06625	906	0,947175	FALSE	1
27	ctx	0,001228	-0,01472	913	0,988253	FALSE	1
27	cal	0,052165	-1,06744	770	0,285775	FALSE	1
28	pyr	0,011287	-0,08098	904	0,935459	FALSE	1
28	ctx	0,044164	-0,24293	882	0,808057	FALSE	1
28	cal	0,092509	-1,37662	728	0,168628	FALSE	1
29	pyr	0,101038	-0,72144	817	0,470639	FALSE	1
29	ctx	0,170768	-2,3778	592	0,017416	TRUE	1
29	cal	0,022345	-0,22644	855	0,820856	FALSE	1
30	pyr	0,039693	-0,1887	860	0,850328	FALSE	1
30	ctx	0,052065	-0,20612	887	0,836693	FALSE	1
30	cal	0,062979	-1,14105	760	0,253848	FALSE	1
31	pyr	0,150898	-0,72144	817	0,470641	FALSE	1
31	ctx	0,009545	-0,41225	859	0,680156	FALSE	1
31	cal	0,064642	-0,9791	782	0,327532	FALSE	1
32	pyr	0,121371	-1,02326	776	0,306184	FALSE	1
32	ctx	0,049128	-0,4785	850	0,632291	FALSE	1
32	cal	0,001371	-0,08834	903	0,929606	FALSE	1

Pat	structure	S-Diff	Z	WSR	p	H	p > 0.0041
33	pyr	0,151458	-1,38767	726,5	0,165239	FALSE	1
33	ctx	0,043826	-0,55948	839	0,575833	FALSE	1
33	cal	0,024535	-0,43434	856	0,664042	FALSE	1
34	pyr	0,038013	-0,36072	866	0,718309	FALSE	1
34	ctx	0,066494	-0,68463	822	0,493578	FALSE	1
34	cal	0,004393	-0,27173	849	0,78583	FALSE	1
35	pyr	0,083556	-0,66254	825	0,507622	FALSE	1
35	ctx	0,093594	-1,1116	764	0,266309	FALSE	1
35	cal	0,100182	-1,31038	737	0,190066	FALSE	1
36	pyr	0,166864	-1,85513	663	0,063578	FALSE	1
36	ctx	0,068153	-0,72144	817	0,470641	FALSE	1
36	cal	0,003332	-0,07362	905	0,941316	FALSE	1
37	pyr	0,275433	-2,20851	615	0,027209	TRUE	1
37	ctx	0,055261	-0,79505	807	0,426583	FALSE	1
37	cal	0,070414	-1,31037	737	0,190071	FALSE	1
38	pyr	0,046416	-0,24293	882	0,808057	FALSE	1
38	ctx	0,045651	-0,71408	818	0,475181	FALSE	1
38	cal	0,106769	-1,72999	680	0,083632	FALSE	1
39	pyr	0,098797	-0,24908	852	0,803295	FALSE	1
39	ctx	0,009883	-0,24293	882	0,808057	FALSE	1
39	cal	0,037013	-0,90549	792	0,365208	FALSE	1
40	pyr	0,100923	-1,03799	774	0,299273	FALSE	1
40	ctx	0,026036	-0,40489	860	0,68556	FALSE	1
40	cal	0,052165	-0,72881	816	0,46612	FALSE	1
41	pyr	0,009046	-0,1887	860	0,850328	FALSE	1
41	ctx	0,042441	-0,25766	880	0,796672	FALSE	1
41	cal	0,041597	-0,43434	856	0,664041	FALSE	1
42	pyr	0,297281	-2,36309	594	0,018123	TRUE	1
42	ctx	0,06268	-0,71408	818	0,475181	FALSE	1
42	cal	0,00873	-0,11042	900	0,912072	FALSE	1
43	pyr	0,050222	-0,75088	813	0,452723	FALSE	1
43	ctx	0,020477	-0,47114	851	0,637539	FALSE	1
43	cal	0,068572	-1,6122	696	0,106918	FALSE	1
44	pyr	0,227814	-1,82568	667	0,067898	FALSE	1
44	ctx	0,002973	-0,11779	899	0,906238	FALSE	1
44	cal	0,112236	-2,38516	591	0,017072	TRUE	1
45	pyr	0,171511	-1,90666	656	0,056565	FALSE	1
45	ctx	0,058537	-0,91284	791	0,361327	FALSE	1
45	cal	0,057283	-0,99383	780	0,320304	FALSE	1
46	pyr	0,167309	-1,34718	732	0,177921	FALSE	1
46	ctx	0,135107	-1,63428	693	0,102201	FALSE	1
46	cal	0,043617	-0,785	781	0,432455	FALSE	1
47	pyr	0,19448	-1,61955	695	0,105328	FALSE	1
47	ctx	0,173684	-1,98763	645	0,046852	TRUE	1

Pat	structure	S-Diff	Z	WSR	p	H	p > 0.0041
47	cal	0,058819	-0,9055	792	0,365203	FALSE	1
48	pyr	0,074707	-0,54476	841	0,58592	FALSE	1
48	ctx	0,024305	-0,01472	913	0,988253	FALSE	1
48	cal	0,08925	-1,72631	680,5	0,084291	FALSE	1
49	pyr	0,108881	-1,16314	757	0,244774	FALSE	1
49	ctx	0,053157	-0,43433	856	0,664045	FALSE	1
49	cal	0,085209	-1,35454	731	0,175564	FALSE	1
50	pyr	0,11801	-0,65519	826	0,512346	FALSE	1
50	ctx	0,01963	-0,11779	899	0,906238	FALSE	1
50	cal	0,050866	-1,29933	738,5	0,193832	FALSE	1

4.3 Comparison to non-tracking group

4.3.1 Output Curves

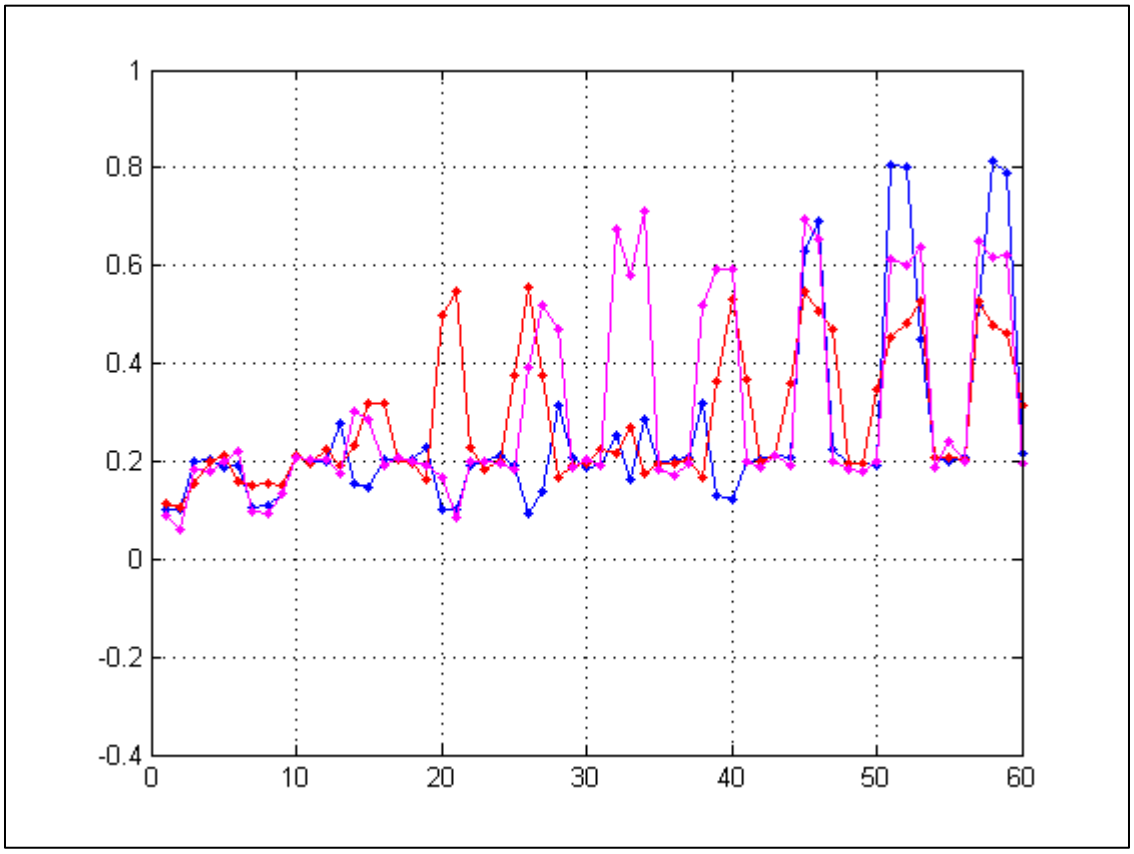

Figure 30. Results curves for Cortex (red), Pyramids (magenta) and Calix (blue)

4.3.1.1 Cortex

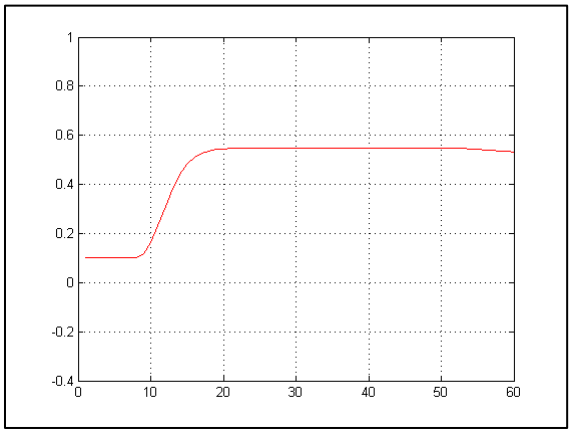

Figure 31. Gamma function curve.

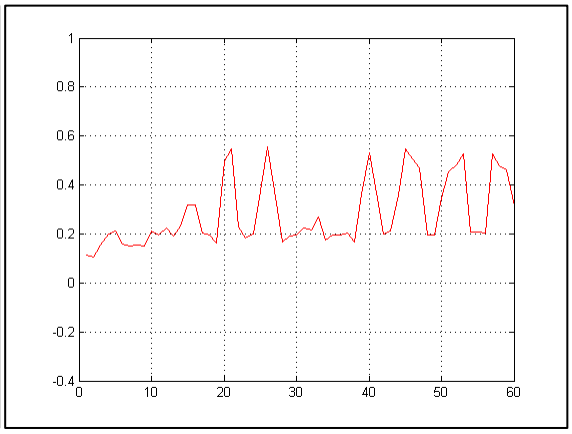

Figure 32. Output curve.

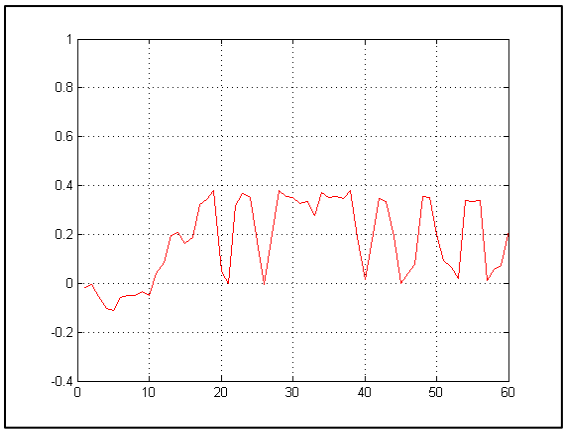

Figure 33. Results comparison curve.

4.3.1.2 Pyramids

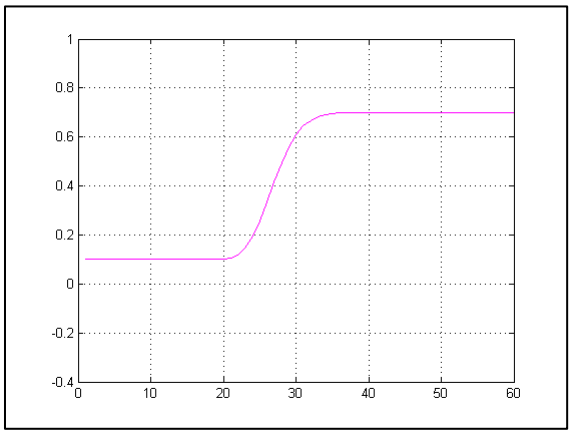

Figure 34. Gamma function curve.

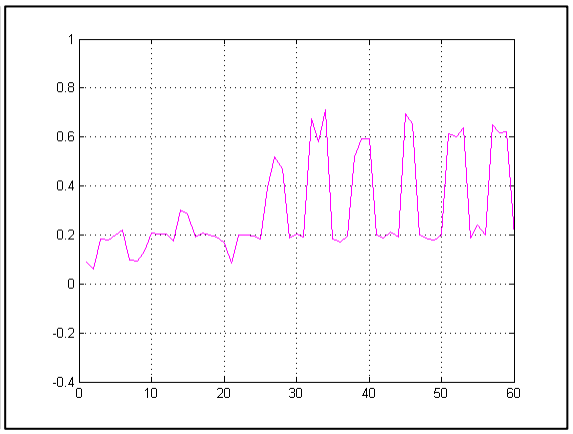

Figure 35. Output curve.

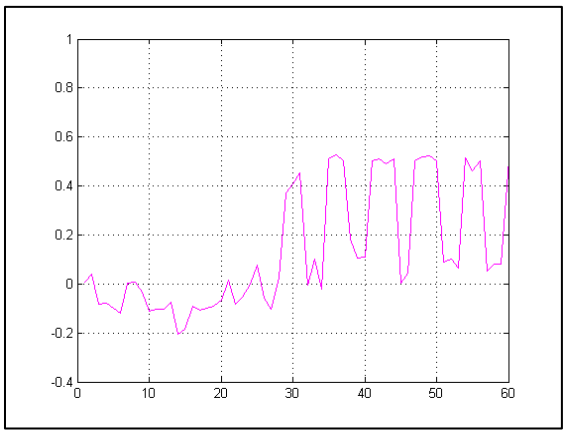

Figure 36. Results comparison curve.

4.3.1.3 Calix

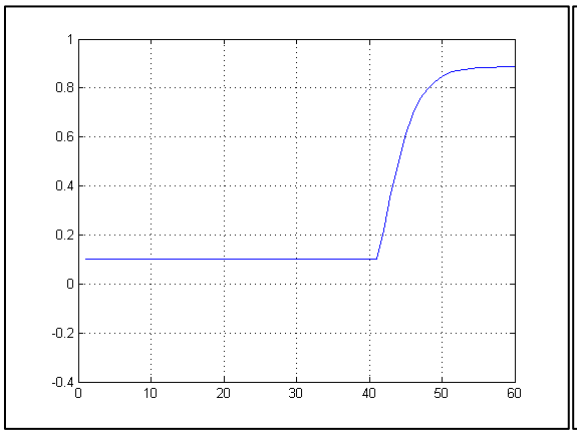

Figure 37. Gamma function curve.

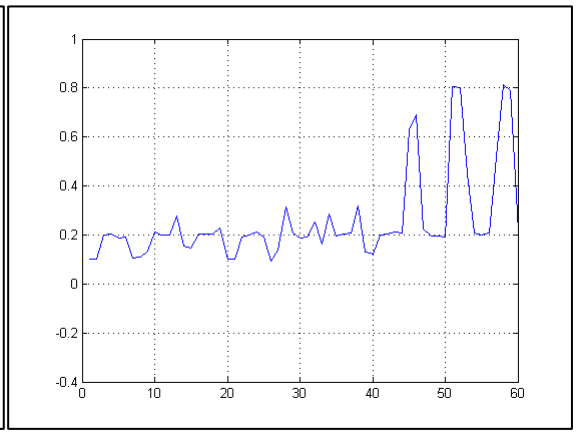

Figure 38. Output curve.

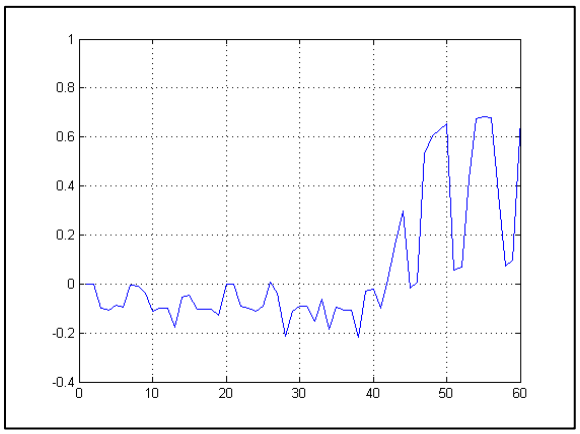

Figure 39. Results comparison curve.

4.3.2 Results table for non-tracking group

The alpha value still equals 0.0041 after correction based on multiple testing. The values in last column in Table 5 show varying p-values, meaning that several comparisons do not meet the criteria of being greater than alpha while others do. Consequently the hypothesis tests become true and the H0-Hypothesis can be rejected. Therefore it cannot be assumed that the test is accurate in its assumption of having a median of zero.

Table 5. Statistical output of non-kidney tracking measurements.

Pat	structure	S-Diff	Z	WSR	p	H	p > 0.0041
1	pyr	8,033416	-2,62809	558	0,008586522	TRUE	1
1	ctx	10,47992	-5,64635	148	1,63891E-08	TRUE	0
1	cal	3,197865	-1,14105	760	0,253848147	FALSE	1
2	pyr	8,200643	-2,7606	540	0,005769509	TRUE	1
2	ctx	10,23002	-5,71997	138	1,06546E-08	TRUE	0
2	cal	3,224247	-1,05271	772	0,292474277	FALSE	1
3	pyr	8,059746	-2,55448	568	0,010634769	TRUE	1
3	ctx	10,44202	-5,6758	144	1,38045E-08	TRUE	0
3	cal	3,458352	-0,95701	785	0,33856302	FALSE	1
4	pyr	7,891119	-2,51032	574	0,012062056	TRUE	1
4	ctx	10,74063	-5,80094	127	6,5943E-09	TRUE	0
4	cal	3,29026	-1,0159	777	0,309676431	FALSE	1
5	pyr	7,863388	-2,63178	557,5	0,008493835	TRUE	1
5	ctx	10,62543	-5,69052	142	1,26654E-08	TRUE	0
5	cal	3,283724	-1,04535	773	0,295862333	FALSE	1
6	pyr	7,832295	-2,53976	570	0,011092804	TRUE	1
6	ctx	10,6735	-5,69052	142	1,26654E-08	TRUE	0
6	cal	2,981347	-1,19995	752	0,230160564	FALSE	1
7	pyr	7,924452	-2,67226	552	0,007534182	TRUE	1
7	ctx	10,72131	-5,74205	135	9,3537E-09	TRUE	0
7	cal	3,235655	-1,06743	770	0,285776608	FALSE	1
8	pyr	8,032015	-2,92256	518	0,003471707	TRUE	0
8	ctx	10,56173	-5,72733	137	1,02025E-08	TRUE	0
8	cal	3,262333	-1,00854	778	0,313193842	FALSE	1
9	pyr	8,155825	-2,77533	538	0,005514509	TRUE	1
9	ctx	10,38799	-5,7715	131	7,85705E-09	TRUE	0
9	cal	3,318186	-1,12633	762	0,26002787	FALSE	1
10	pyr	8,636497	-2,95201	514	0,003157098	TRUE	0
10	ctx	10,23772	-5,6758	144	1,38045E-08	TRUE	0
10	cal	3,272791	-1,06743	770	0,285776608	FALSE	1
11	pyr	8,124172	-2,8563	527	0,004286073	TRUE	1

Pat	structure	S-Diff	Z	WSR	p	H	p > 0.0041
11	ctx	10,52237	-5,6758	144	1,38045E-08	TRUE	0
11	cal	3,011769	-1,11897	763	0,263154027	FALSE	1
12	pyr	8,721371	-2,92992	517	0,003390515	TRUE	0
12	ctx	10,23508	-5,68316	143	1,3223E-08	TRUE	0
12	cal	3,417473	-1,02327	776	0,306181961	FALSE	1
13	pyr	7,86899	-2,60602	561	0,009160211	TRUE	1
13	ctx	10,54697	-5,7126	139	1,1126E-08	TRUE	0
13	cal	3,31783	-1,03799	774	0,299273289	FALSE	1
14	pyr	7,764788	-2,46615	580	0,01365759	TRUE	1
14	ctx	10,73213	-5,70524	140	1,16178E-08	TRUE	0
14	cal	3,300123	-1,0159	777	0,309676431	FALSE	1
15	pyr	8,290279	-2,96673	512	0,003009891	TRUE	0
15	ctx	10,33576	-5,55801	160	2,72867E-08	TRUE	0
15	cal	3,031199	-1,03799	774	0,299276562	FALSE	1
16	pyr	8,102043	-2,70909	547	0,006746839	TRUE	1
16	ctx	10,61416	-5,72733	137	1,02025E-08	TRUE	0
16	cal	3,342013	-1,05271	772	0,292472643	FALSE	1
17	pyr	8,202603	-2,92256	518	0,003471707	TRUE	0
17	ctx	10,4374	-5,60218	154	2,11673E-08	TRUE	0
17	cal	3,230842	-1,06007	771	0,289112376	FALSE	1
18	pyr	8,114648	-2,88575	523	0,003904842	TRUE	0
18	ctx	10,64003	-5,63163	150	1,78518E-08	TRUE	0
18	cal	3,230129	-1,1705	756	0,24180028	FALSE	1
19	pyr	8,353584	-2,95937	513	0,003082643	TRUE	0
19	ctx	10,28549	-5,77886	130	7,52092E-09	TRUE	0
19	cal	3,284021	-1,0748	769	0,28246532	FALSE	1
20	pyr	8,302323	-2,67963	551	0,007370301	TRUE	1
20	ctx	10,25611	-5,69788	141	1,21306E-08	TRUE	0
20	cal	3,503332	-0,9791	782	0,327532293	FALSE	1
21	pyr	7,682996	-2,32627	599	0,020004335	TRUE	1
21	ctx	10,61391	-5,74205	135	9,3537E-09	TRUE	0
21	cal	3,244152	-1,04535	773	0,295862333	FALSE	1
22	pyr	8,009606	-2,59865	562	0,009359227	TRUE	1
22	ctx	10,52217	-5,73469	136	9,76916E-09	TRUE	0
22	cal	3,413136	-0,99382	780	0,320312258	FALSE	1
23	pyr	8,132575	-2,76796	539	0,005640791	TRUE	1
23	ctx	10,50604	-5,64635	148	1,63891E-08	TRUE	0
23	cal	3,41171	-1,00119	779	0,3167342	FALSE	1
24	pyr	7,928094	-2,73116	544	0,006311106	TRUE	1
24	ctx	10,68811	-5,63163	150	1,78518E-08	TRUE	0
24	cal	3,336011	-1,0159	777	0,309676431	FALSE	1
25	pyr	7,89308	-2,65018	555	0,008044959	TRUE	1
25	ctx	10,68752	-5,69788	141	1,21306E-08	TRUE	0
25	cal	2,866909	-1,2662	743	0,205443021	FALSE	1

Pat	structure	S-Diff	Z	WSR	p	H	p > 0.0041
26	pyr	8,028374	-2,71643	546	0,006598985	TRUE	1
26	ctx	10,60106	-5,7126	139	1,1126E-08	TRUE	0
26	cal	3,20553	-1,21467	750	0,22449251	FALSE	1
27	pyr	8,302884	-2,92257	518	0,003471597	TRUE	0
27	ctx	10,37429	-5,74941	134	8,95544E-09	TRUE	0
27	cal	3,276297	-0,91284	791	0,361327343	FALSE	1
28	pyr	8,413808	-2,88575	523	0,003904842	TRUE	0
28	ctx	10,45459	-5,74205	135	9,3537E-09	TRUE	0
28	cal	3,3943	-1,0159	777	0,309676431	FALSE	1
29	pyr	8,162828	-2,77532	538	0,005514668	TRUE	1
29	ctx	10,40964	-5,73469	136	9,76916E-09	TRUE	0
29	cal	3,258352	-1,00855	778	0,313192203	FALSE	1
30	pyr	8,038178	-2,79005	536	0,00527003	TRUE	1
30	ctx	10,57457	-5,65371	147	1,5702E-08	TRUE	0
30	cal	3,243557	-1,14841	759	0,250797714	FALSE	1
31	pyr	8,609046	-2,8003	514	0,005105528	TRUE	1
31	ctx	10,2131	-5,69788	141	1,21306E-08	TRUE	0
31	cal	3,377307	-1,05271	772	0,292474277	FALSE	1
32	pyr	8,313248	-2,952	514	0,003157201	TRUE	0
32	ctx	10,22842	-5,75677	133	8,57368E-09	TRUE	0
32	cal	2,901252	-1,25884	744	0,208088716	FALSE	1
33	pyr	8,282715	-2,93728	516	0,003311054	TRUE	0
33	ctx	10,36638	-5,76414	132	8,20776E-09	TRUE	0
33	cal	3,279624	-1,04535	773	0,295860697	FALSE	1
34	pyr	8,060587	-2,82686	531	0,004700753	TRUE	1
34	ctx	10,50506	-5,70524	140	1,16178E-08	TRUE	0
34	cal	3,315393	-1,04535	773	0,295862333	FALSE	1
35	pyr	8,365068	-3,00354	507	0,002668548	TRUE	0
35	ctx	10,29933	-5,74205	135	9,3537E-09	TRUE	0
35	cal	3,292399	-0,9791	782	0,327532293	FALSE	1
36	pyr	7,967589	-2,49558	576	0,012575018	TRUE	1
36	ctx	10,77848	-5,74205	135	9,3537E-09	TRUE	0
36	cal	3,177069	-1,24411	746	0,213458747	FALSE	1
37	pyr	8,397001	-2,69435	549	0,007052676	TRUE	1
37	ctx	10,08894	-5,72733	137	1,02025E-08	TRUE	0
37	cal	3,17184	-0,94229	787	0,346043384	FALSE	1
38	pyr	8,504564	-2,99617	508	0,002733918	TRUE	0
38	ctx	10,27276	-5,69052	142	1,26654E-08	TRUE	0
38	cal	3,279683	-1,03799	774	0,299274925	FALSE	1
39	pyr	7,84406	-2,59865	562	0,009359227	TRUE	1
39	ctx	10,7848	-5,73469	136	9,76916E-09	TRUE	0
39	cal	3,247954	-1,13369	761	0,256925922	FALSE	1
40	pyr	8,303444	-2,65755	554	0,007871145	TRUE	1
40	ctx	10,72285	-5,77886	130	7,52092E-09	TRUE	0

Pat	structure	S-Diff	Z	WSR	p	H	p > 0.0041
40	cal	3,446231	-1,0159	777	0,309676431	FALSE	1
41	pyr	8,260307	-2,92258	518	0,003471487	TRUE	0
41	ctx	10,20972	-5,6758	144	1,38045E-08	TRUE	0
41	cal	3,212066	-1,03799	774	0,299276562	FALSE	1
42	pyr	8,063388	-2,63545	557	0,008402484	TRUE	1
42	ctx	10,66762	-5,81567	125	6,03928E-09	TRUE	0
42	cal	3,222821	-1,1116	764	0,266309289	FALSE	1
43	pyr	8,663108	-2,82687	531	0,004700612	TRUE	1
43	ctx	10,14803	-5,69788	141	1,21306E-08	TRUE	0
43	cal	3,455203	-1,00854	778	0,313193842	FALSE	1
44	pyr	8,278514	-2,92993	517	0,003390406	TRUE	0
44	ctx	10,59181	-5,69052	142	1,26654E-08	TRUE	0
44	cal	3,219196	-1,08952	767	0,275925855	FALSE	1
45	pyr	8,035657	-2,66444	532	0,007711765	TRUE	1
45	ctx	10,5533	-5,78622	129	7,19879E-09	TRUE	0
45	cal	3,396202	-0,94965	786	0,342291757	FALSE	1
46	pyr	8,131455	-2,69435	549	0,007052676	TRUE	1
46	ctx	10,58268	-5,66843	145	1,44108E-08	TRUE	0
46	cal	3,250985	-1,13369	761	0,256925922	FALSE	1
47	pyr	8,422211	-3,0477	501	0,002305972	TRUE	0
47	ctx	10,37499	-5,79358	128	6,8901E-09	TRUE	0
47	cal	3,242607	-1,22203	749	0,221696193	FALSE	1
48	pyr	8,136497	-2,8563	527	0,004286073	TRUE	1
48	ctx	10,72802	-5,69052	142	1,26654E-08	TRUE	0
48	cal	3,274633	-1,01591	777	0,309669876	FALSE	1
49	pyr	8,0942	-2,68699	550	0,007209821	TRUE	1
49	ctx	10,63731	-5,68316	143	1,3223E-08	TRUE	0
49	cal	3,192399	-1,19258	753	0,233034025	FALSE	1
50	pyr	8,06927	-2,83422	530	0,00459381	TRUE	1
50	ctx	10,56344	-5,62426	151	1,863E-08	TRUE	0
50	cal	3,351222	-1,08216	768	0,279183375	FALSE	1

4.3.3 Result comparison

Comparing the output curves between the tracking and non-tracking group it becomes evident that a more stable analysis was conducted in the tracking group. Even if the original gamma functions can be suspected at the curve maximum, the data points in between do not always contain compartment information as the kidney may be out of bounds. If the non-tracking group were meant to portray respiratory gating, only the results along a discerned and discontinued gamma curve would be eligible for evaluation, managing to exemplify the reduced level of information compared to the tracking group.

5. Discussion

5.1 Introduction to discussion

In this dissertation a software based simulation was performed to automate the analysis of functional MR Urography images. Using Matlab we managed to generate image series with simplified versions of fMRU images, consisting of a moving kidney being injected with contrast agent. Our goal was to analyze the change in contrast agent intensity over time in the different compartments of the kidney, without having to manually define the respective areas of interest in each image. As this simulation stands firm under statistical scrutiny, we can conclude that our hypothesis has been successfully verified. This opens up for the possibility of forming the foundation for further research in automated image analysis of renal function assessment.

5.2 Critique of methods

5.2.1 Generation of data

Image background

Several aspects of the generated images have been reduced in complexity in comparison to real fMRU scans. One of the most obvious differences lies in the fact that there are no background structures present in the images. Instead a greyscale color with an overlay of simulated noise is acting as canvas, replacing organs and anatomy usually found in these kinds of scans. Spleen and liver are absent, as are blood vessels, fat and muscles. This is probably the most significant difference compared to real life scans, which enables the program to focus on one single object without having to determine if this is in fact the sought after kidney. If other structures would be present in the picture, the current functions of the program would try to eliminate the identified object until the largest one remains. This would not necessarily mean that the kidney be recognized as such, but that the liver or even the spleen might be mistakenly identified as the kidney to later be tracked. Additional structures might also lead to an incorrect localization of the kidneys extreme points that would lead to placement of the borders with either too much or too little marginal.

Singular kidney and orientation

The vertebrae column which separates the right and left kidney from each other is also missing, shining light on a further simplification: there is only one kidney visible. Whereas an additional kidney would have been neither difficult to add nor analyze, the new data might come at the cost of computational efficiency, unnecessarily slowing down the generation of images. The same input curves for the gamma functions would have been used, changing little more than the complexity of the simulation. Writing code to enable the program to determine left or right sided orientation of the kidneys would also not have been an obstacle. It would only translate into an increased consumption of processing power better reserved for other functions.

Kidney variation

When comparing the image series to each other, it becomes obvious that the kidneys never change in size or shape. The same elliptical dimensions are applied to all simulated patients, making the starting coordinates for the first frame the sole source of variance. In real life every patient would have kidneys of different size and shape including individual and thereby varying location inside the situs. While a reduction in variability puts the simulation further away from real life conditions, this becomes an acceptable compromise as the main focus is kept on the identification of the kidney. In contrast to the simplified anatomy stands the exaggerated movement of the kidney, where the simulation depicts a kidney that moves a vertical distance of more than its own length. While not plausible in real life this allows for thorough evaluation of the tracking routine of the program.

Anatomical detail

Maintaining a certain level of detail while trying not to end up with an unnecessarily complex simulation inevitably leads to compromise. The level of anatomical detail of the kidney has been reduced to three distinct compartments. They comprise of the outmost lying cortex enveloping three pyramid shaped forms representing the medullae, from where the urine is drained into the renal pelvis. Firstly the number of pyramids is greatly reduced to three instead of the more common range of upper twenties. Besides the fact that 30 pyramids would not have fitted inside our simplified kidney, it would have been difficult to assign the equal amount of regions of interest on the current limited space. Our solution of three larger medullae oriented along the left central region of the kidney seems like a simplified but sensible tradeoff. This led to another compromise as we realized that the measurement of the

cortex could not be reliably performed along its circumference. Instead we used two separate masks to measure intensity change on the upper and lower poles of the kidney, as there were no interfering structures present in that area. Even though the area to be measured is very limited the statistics show that it is sufficient for data retrieval and evaluation. This was a main concern when writing the code for the images. If there are too few pixels to be measured, every change in pixel intensity will lead to great differences in the measured value, giving the noise layer too much influence. One plausible solution would have been to increase image size by a certain factor, yielding additional pixels and data to be evaluated. This would however have reduced the similarities with real life MR images where the scan matrix is also relatively small, a compromise we were not willing to make.

Efficiency

Analyzing the efficiency of the programs image generation the biggest culprit becomes the initial elliptical function for the body of the kidney. To get this output a three-dimensional function is used where the depth of the ellipse is limited to one pixel. The resulting output is definitely satisfactory but begs the question if another function based on two-dimensional coordinates would not have been more meaningful. As this was one of the first parts of the program to be completed the attention was directed towards unfinished aspects of the code, judging that as long as it fulfilled its task the efficiency factor could be ignored until further progress had been made.

5.2.2 Analysis of data

Filters

Starting point for analysis of the generated images is the identification and isolation of the kidney. In order for the program to accurately detect the kidney several filters have to be applied in a specific order, ending up with a binary image where the pixels of the object have the value one, the background pixels value zero. Finding the correct parameters with which the filters were applied was difficult and time consuming, resulting in a prolonged period of trial and error. Applying the initial smoothing could not be too intense, otherwise reducing level of detail below acceptable limits. Not adjusting enough meant ending up with additional objects originating from noise pixels of the background layer. An improvement would have been to analyze the image and try to come up with individual parameter values for each

image. This would have been difficult to realize, requiring an additional experimental phase for which there was simply not enough time. Keeping in mind that the goal at this stage is to isolate the kidney, these initial filters can be applied with fixed parameter values. As long as background properties do not fluctuate into extremes the outcome will always remain the same, omitting the need for adaptive filter strength.

Another function was able to remove binary objects that did not meet the required minimum amount of pixels. Contrary to previous parts of the script, this filter was set to automatically remove smaller objects until only one remained, presumably the kidney. In this context, an obstacle was revealed to be the image border. The algorithms of the filter worked in such a way that pixels on the edges of the image were preferably left together. Those pixels added up and could sometimes become the biggest object thus being identified as the kidney. Fortunately the appropriate function already existed to remove all objects adjacent to the border of the image, effectively solving the problem. Reviewing the motion of the kidney, this correction creates another limitation for the simulation in that the kidney may not move outside of or traverse the edges of the image. As this was not the case no further corrections had to be made.

Border frame

In earlier versions of the program the outer borders of the kidney was recalculated for each image frame, believing this would lead to more exact measurements of the edges. This approach proved to be more difficult than anticipated as the program cannot any longer detect the cortex when it changes intensity from dark to bright. The program then only identifies the areas of the kidney that are still dark, i.e. the pyramids and the calix, resulting in outer borders that do not contain the whole kidney. Somehow this had to be corrected, and the simplest solution was to keep the original outer dimensions from the first frame, assuming the program had managed to identify the right size of the kidney from the beginning. In effect this resulted in a static frame that does not change size as the simulation progresses, but instead the anchor for this frame becomes the central pixel coordinate that is simultaneously calculated for each frame. The question then becomes if the central pixel is always calculated to be in the middle of the kidney, making the placement of the static frame a straightforward task? Unfortunately this is not the case as the changing of intensity of the pyramids occurs later than the cortex, shifting the central point to the left side of the kidney where the majority mass is located. Trying to solve this problem would probably have required a different approach where the use

of binary images would have been neither practical nor possible. Rather the use of pattern recognition could have been explored, but that would have involved the creation of pattern databases as well as developing a new code base, both of which would have exceeded the timeframe for this dissertation. Instead the solution was to limit kidney tracking along a vertical line while keeping the initial horizontal central coordinate for the duration of the simulation. This resulted in a significant limitation of the simulation, but as the kidney is still identified and correctly isolated other options are reserved for future improvements. Only sign left behind of this adjustment is a slight vertical shift of a few pixels of the kidney in relation to the outer frame. It was possible that this could have had a significant impact on measurements but proved not to be the case.

ROI placement

Placement of the regions of interest is done based on the extreme coordinates of the border frame. This was done by experimenting with test code to see how well these masks fitted inside their respective regions. Once the right size and position was found, it was a matter of applying the masks in relation to the kidney edges, instead of assigning fixed coordinates. Herein lies another limitation in the program, namely that the size of the kidney may not fluctuate too extensively, otherwise resulting in suboptimal placement of the measurement masks. As the images are limited in their spatial resolution the regions of interest have to be adapted accordingly, leaving a small margin of error. This may not have bigger impact on real MR images where interpolation increases the amount of measurable pixels, but in our simulation this proved to be an area of detailed calibration. Partial solution was to change the number of masks for the cortex, thereby increasing the amount of pixels for each region, after which their mean values are calculated. Similar actions were not necessary for the calix as the available amount of pixels in one and the same region sufficed for the program to calculate exact values. Even though the region of interest for the pyramids is the smallest in size, additional masks did not have to be added. This seems contra intuitive but test results indicated that the measurements were stable enough in the pyramid, whereas a sole mask on one of the extreme poles of the kidney cortex probably were too close to the outer edges. Cortex masks could have been shrunk in size to avoid being out of bounds, simultaneously risking a too significant reduction in data retrieval.

Noise layer

To increase the similarities of this simulation with real life MR scans a layer of noise was

added to the images. Even though this seemed trivial at first, several adjustments had to be made as the experiment progressed. It was not possible to add a layer of randomized values ranging from 0 to 0.1 (10%) as this would increase the offset of the whole interval by 10%. As the upper boundary is 1, this means that all values added to pixels already possessing the value 1 would be lost. The answer was to add a randomized number ranging from -0.1 to 0.1 to each pixel, solving uniform distribution but leaving the changed interval an unsolved problem. Lower and upper boundaries would still ignore subtraction from zero or addition to one, limiting and explaining the measurement of brightness intensity to an interval between 0.1 and 0.9 as shown in the graphics. Input gamma curves were adjusted after this discovery thus letting the program function properly without the need for manual adjustment later on.

Efficiency

When the program is running it looks as if the measurement of the regions of interest is done in real time. This is only partly correct as some of the data has been pre cached prior to execution. After generating the images an additional script is run that identifies the kidney in its binary format, extracts the border frame coordinates and crops the kidney from the original picture. Ending up with a new image series containing the now motion stabilized kidneys, the intensity change over time is measured on these without utilizing additional processing power. Advantages can be seen when comparing this to thumbnail rendering on computers. These are created temporarily each time a folder with image files is opened, using processing power but saving disk space. In this simulation we did not see any limitations in disk space but preferred the increased efficiency in image analysis. During the course of this dissertation this method has been the greatest contributor in terms of improving time efficiency.

Patlak plot requirement

Early attempts to measure separate compartment changes were difficult to realize. One of the first approaches involved creating exact masks that matched the kidney circumference to the pixel. This proved problematic as it was not possible to clearly differentiate between individual compartment changes where all three output curves from the gamma function were superimposed on each other. In reality one would have to solve complex patlak equations, which a computer would be able to calculate. For this to be possible a requirement is that the contrast agent is not allowed to leave the renal parenchyma, meaning an end to the measurements as soon as contrast agent is detected in the calix. Therefore the need to be able to differentiate between different compartments of the kidney was not strictly necessary for

successful completion of our simulation, but a significant factor in terms of realism when comparing to real world conditions and application. This forced us to consider alternative options whereupon we started experimenting with static regions of interest. Early results showed promise and the method was refined until statistics could be presented with reliable data.

5.3 Results

Measured intensities are plotted in graphs which are then compared to the original input gamma curves. Following subtraction from the input curves a second curve of differences is acquired which is then analyzed using the Wilcoxon signed rank test and later adjusted with Bonferroni correction. If the measurements were to be performed perfectly the curve of differences would be a straight line along the median of zero. As seen in the graphs for each compartment this is not the case which may be explained by multiple factors.

ROI placement

Most obvious source of error is inaccurate placement of regions of interest on the compartments of the kidney. This may be true to some extent as the tracking box visualizing a magnified and movement-stabilized version of the kidney shows slight stuttering in the vertical axis. Closer inspection shows that the masks are inside said regions for the length of the simulation, showing occasional extremes where the edges of the masks contact the pixels on the border. This is best visualized when viewing the output graph for the pyramids, showing distinct fluctuations along its original trajectory. Probable explanation for this phenomenon lies in the fact that the mask for the pyramid is the smallest one compared to the amount of pixels in the remaining regions of interest. Found motion stuttering would impact measurements on this area, whereas the remaining masks are not affected to the same degree owing to greater data sample.

Noise

Another explanation for inaccuracies could be attributed to the added layer of noise, designed to make the simulation more similar to real world conditions. Analogous to the previous explanation with small sample sizes, noise has the ability to distort measurements if the amount of pixels are too few. This can be seen in all of the output graphs where instead of a

smooth measurement curve the noise is represented by a distinctly jagged curve. As long as this noise is evenly distributed along the curve without extreme exceptions the statistical t-test will not regard this as a flaw in the experiment.

Compartment preference

One interesting aspect when trying to explain possible statistical deviation in this dissertation is to determine if there are any distinct differences between compartment measurements. From 150 compartment measurements only eight show statistical nonconformity in that the curve possessing a median of zero cannot be safely assumed. These eight compartments are comprised of three calix, three cortex and two pyramid measurements, showing an even distribution over all compartments with z-values between -1.97 and -2.3. Even though the mask for the pyramid is smallest in size the equivalent measurements are shown to be slightly more accurate than for cortex or calix regions. Going against previous assumptions where small masks for the pyramid were thought to lead to greater irregularities, this could be explained by the nature of the Wilcoxon T-test where curve amplitude becomes less important than distribution of irregularities.

Wilcoxon signed rank test

An important parameter of the Wilcoxon signed rank test is the calculated standard deviation which establishes the limits for rejection of the null-hypothesis. Shown by the associated z-value representing the amount of standard deviations, z may not exceed the boundaries of below -1.96 or above 1.96, otherwise resulting in rejection of the null-hypothesis. For this to occur the plotted line would need to possess outliers with a magnitude exceeding the defined amount of standard deviations. This means that successful outcome of the wilcoxon signed rank test does not consider amplitude of the graph as long as the values are evenly distributed around the median line. A graph with regular oscillations and amplitudes of 10 units is more probable to pass the wilcoxon signed rank test than a more detailed plot with amplitudes of 1unit possessing an outlier with the amplitude of 10 units. Despite the latter graph generally being more accurate than the former, statistically this would indicate a failed measurement. This might partly answer the question of why the measurements of the pyramid compartments are often successful regardless of their relatively small size.

Bonferroni correction

As previously mentioned the phenomenon of multiple testing allows us to utilize a modified

value of alpha. By use of Bonferroni correction the new alpha becomes 0.0041 which is compared to the p-values in table 4 and 5. In total, eight of 150 measurements (5.33%) do not hold up to the desired significance level of 0.05 which would otherwise have resulted in a failed experiment, were it not for the bonferroni correction. Problem of bias towards graphs with irregularly plotted lines but evenly distributed along their course is hereby partly compensated. Amplitude becomes a less important factor letting the eight graphs with otherwise exact measurements but singular outliers become statistically valid.

5.4 Comparison of modalities and kidney tracking methods

fMRU contextualized

Despite distinct advantages of MR urography compared to more conventional methods of renal function assessment, MR imaging is not always the preferred modality. Standard laboratory results are important in everyday clinical operations and may allow for an estimation of kidney function by eGFR values (8). More accurate methods have to be used if the kidneys are to be assessed individually, as well as when morphological information is required, giving fMRU the upper hand (16). Whereas the results of blood and urine samples can be had in a matter of hours, the process of collecting urine for 24 hours cannot be further optimized, making fMRU another viable candidate when time is of the essence.

Nuclear medicine has an established position in the assessment of renal function. Scan times do not have to exceed the one hour mark, but preparations tend to extend the process (64). Compared to fMRU, renal scintigraphy lacks in spatial resolution (17), (22). This keeps information gain limited to kidney function but with the upside that respiratory gating becomes redundant. Once again pointing out the use of ionizing radiation further adds to the restrictions of nuclear imaging. In both instances sedation could become necessary when children are involved.

Most of the methods discussed in this dissertation require a substantial amount of time for either preparation, scan time or post processing. Even though sonography is not used to depict kidney function in a standardized fashion over a longer time span, it is the go to method when a quick evaluation of the kidneys has to be made. Voiding urosonography can shed light on possible vesicoureteral reflux (37). Urolithiasis as well as congenital anomalies can get an initial assessment, even perfusion can be imaged with Doppler technique, becoming

especially important in kidney transplants (31)(38). In general no sedation is necessary but results may vary greatly depending on the experience of the examiner. With the improvements of contrast agent developed for sonography even functional diagnosis may become viable (36). Until then fMRU remains a method with predefined protocols, making standardized evaluation of kidney function possible across a diverse set of hardware with varying operator expertise.

The only real contender to fMRU in terms of anatomical resolution is computed tomography with its superior spatial contrast resolution (16). This modality is not a realizable alternative to fMRU when kidney function is to be evaluated as the high doses of radiation cannot be justified. In a similar fashion to renal fluoroscopy, alternative methods like fMRU that do not involve radiation are constantly improved on, making it a question of time before new standards are established.

An argument against MR imaging is the prolonged duration of the scan. This means that patients which could hypothetically be diagnosed with the help of this technique have to be assessed, trying to conclude if a MR scan could prove beneficial in terms of more accurate diagnosis. Even though a diagnosis could be made with MR imaging, in a clinical setting with limited resources more severe cases must be prioritized, forcing patients to use alternative modalities. Simply put, MR imaging may not be able to meet patient frequency demand even though said examination would be indicated or even preferred, leading to long waiting times. Inevitably linked to the extensive time frame of MR imaging are costs of running the machine and employment of staff capable of operating the scanner. These time-dependent variables cannot be optimized indefinitely, as the duration of the scans are limited by the physiology of the kidneys. However, every measure devoted to reduction of scan time and post-processing workload may therefore increase the possibility of using MR imaging in place of more conventional techniques.

Kidney Motion Correction and Segmentation

Automation of image analysis has become an increasingly important subject as technological possibilities expand and data volumes continue to grow. In 1991 Gerig et al. tried to optimize alignment in dynamic MR images from 20 studies taken in breath-hold technique, where an algorithm searched for manually predefined kidney contours (65). This sort of template matching utilizing Hough transformation required distinct and rigid kidney contours but

allowed for rotational and size variance. Contrary to our method, manual steps where still necessary but the process of kidney registration could be reduced from several hours to 30-50 minutes in total. De Priester et al. used a different approach in 2001 involving transplanted kidneys, thereby removing the need for motion correction (66). The method involved automated subtraction of non contrast-enhanced from enhanced dynamic MR images, but still needed manual intervention to exclude kidney hilar area from ROI. Our approach, using automated object recognition in a software model, did not rely on manually drawn organ contours and was especially designed to equalize the impairment of image quality due to respiratory motion.

Even though breath-hold techniques help reduce motion artifacts in MR imaging, experiments confirmed that the diaphragm does not remain stationary during this time (67). Trying to assess which movement correction technique was most successful, Giele et al. in 2001 compared three methods making use of either image matching, cross correlation or phase difference movement detection (PDMD) with Fourier transformation (68). All methods required initial manual drawing of contours to create a binary mask that is then used to search for kidney features in remaining images. Even though the PDMD method showed the most favorable results, a fully automated solution was not realizable.

A year later Sun et al. investigated the topic of automated kidney registration and segmentation in multiple papers, starting with analysis of transplanted kidneys in rats, ignoring the obstacle of breathing motion (69). Their algorithm could identify motion free kidneys based on temporal intensity change (energy based image segmentation) not unlike the methods discussed by de Priester. In 2004 Sun et al. developed a method to counter breathing motion that is invariant to rapidly changing contrast (70). Large scale motion is identified by template matching based on image gradient between kidney parenchyma and surrounding tissue. Once again the disadvantages included the need for strong kidney edges as well as initial manual crop of kidney area. The same algorithm for kidney segmentation was used later the same year in an attempt to automate motion correction with a subpixel level of accuracy, where intensity changes from bolus injection of contrast agent are differentiated from intensity changes due to motion and noise (71). In contrast, Rusinek et al. in 2007 utilized a graph-cut method for segmentation where “seeds” have to be manually placed on kidney cortex to serve as coordinate anchors, managing to reduce segmentation time from 2,5 hours to 21 minutes (72). While this method is not realizable in everyday clinical situations

due to its invasive nature, the seeds as anchors can be compared to manually drawn contours when evaluating MR images, as done with the CHOP-fmru software developed in 2010 (23). Manual intervention was not possible to overcome.

In 2009 Tang et al. tried a different method to kidney segmentation on a stationary kidney where prior knowledge of the sought after organ shape together with intensity and spatial information is used (73). A Co-focus Elliptical Kidney Model (CEKM) tries to extract the kidney features by fitting two ellipses that share a common focus inside the kidney cortex. Problems arise when cortex is damaged or abnormally formed. Continued work of Tang et al. tries to segment the kidney as well as its compartments by integrating a knowledge based framework into the process (74). It uses previous information about kidney properties, such as shape, size, texture and intensity to identify the kidney with the possibility to extend said database with every new image series. These methods required a stationary kidney free of breathing motion but presented an interesting solution to kidney anatomy variation.

In 2013 Merrem et al. tried to stabilize kidney motion by utilizing a variational calculation scheme, as proposed by Chefd'hotel et al. in 2001, to align images with both rigid and non-rigid registration (75)(76). Through an iterative process, an image is compared to the next in the image series and transformed until alignment is achieved. Still, the patients were asked to hold their breaths between image acquisitions. In four out of five image series, it was possible to stabilize remaining breathing movement. Also in this paper, the multitude of different registration algorithms for the kidney are mentioned, commenting on the absence of a study evaluating which one would be the optimal choice. Compared to our experiment, segmentation was not part of their investigation.

5.5 Impact on praxis and currently used methods

Several factors limiting the accuracy of kidney tracking have been discussed and in a clinical setting sensitivity and specificity have to be able to meet certain requirements. As this is a proof of principle dissertation, reality parameters have been scaled back to assess if, assuming further development, this might become a viable method for kidney function assessment. We have shown that object-recognition based automated tracking and a subsequent measurement of kidney perfusion with contrast agent is possible, resulting in improved data yield and

reduction of manual post processing adjustments.

Breath-holding techniques are commonplace in medical imaging settings, with the benefit of stationary kidneys. While reducing motion artifacts and generating high quality images, Holland et al. could show that the diaphragm is not motionless even when holding ones breath (67). In combination with the fact that temporal resolution is reduced and unrealistic to realize in infants and young children, this justifies the search for methods where kidney function can be assessed without involving breath-hold techniques, such as presented in this dissertation. Not only would examination protocols become more efficient without respiratory gating, the evaluation would become more accurate as tools for correction of breath-induced kidney movement are not readily available in current software.

Reviewing the list of previous research one can conclude that many different approaches to automation of kidney registration and segmentation have been tried. As mentioned by Merrem et al. there does not exist a comprehensive assessment of different tracking methods, making it difficult to move the research in a conclusive direction (75). In the same spirit, methods have been used in all possible combinations, some using stationary kidneys to experiment with segmentation, others ignoring the segmentation in order to focus on organ tracking. Sometimes breath-hold techniques have been employed, other times the absence of movement has been assumed. To our knowledge, to this date no one has been able to compile these methods into a complete package capable of both kidney registration and segmentation at the same time, without requiring additional manual intervention. Our approach adds an important idea to the scientific discussion, as we did not register entire images, but restrained computational work to a subset image, identified by object recognition.

While we have managed to track the kidney in our dynamic MR imaging series, extraction time-intensity-curves were based on fixed coordinates, leaving little room for anatomical variance. If work on our program were to continue with the goal of a one stop solution for fMRU imaging evaluation, future improvements would have to overcome the obstacle of more complex anatomy where the kidney and its compartments have to be successfully and accurately identified. Adaptation to more flexible and complex methods as discussed in this dissertation would be required, where the most promising alternative remains to be seen. Methods could be based on finding the area in an image where brightness intensities show greatest change over time, i.e. energy based image segmentation as used by Rusinek et al. and

Sun et al. (72)(69)(70)(71). Often some kind of contour detecting algorithm has to be utilized such as described by Gerig et al. and Giele et al. (65)(68).

Manual observation and adjustment will much likely still be necessary when computer analysis does not meet a certain level of confidence, which could be the case when scanning patients with extensive renal anomalies. In those cases software where manual input is required will still see its use. Methods as discussed by Rusinek et al. where kidney tissue has to be defined manually already exist in programs like CHOP-fMRU, that requires input for regions of interest to specify possible damaged tissue and following segmentation (72)(23). Exciting new possibilities are discussed by Tang et al. where a database containing information about kidney position probability and shape helps in identifying the kidneys (73). Developing this idea further to incorporate a self-learning platform to extend an ever growing database, also discussed by Tang et al., would further refine tracking accuracy (74). It would be possible to build a database with MR urography scans, where a program could try to match forms to each other, determining kidney anatomy empirically. As computer sciences and image processing evolves, new methods may be revealed.

5.6 Summary

Functional Magnetic Resonance Urography has emerged as a viable option to some of the more established imaging modalities currently used for diagnostics in medicine. Contributing factors include absence of ionizing radiation as well as a low frequency of undesirable side effects from contrast agents, allowing for more specific examination in patients with relative or absolute contraindications to conventional methods. Considering the temporal resolution of fMRU scans, the impact of motion artifacts on the image quality becomes obvious. Methods to overcome this obstacle have been realized in forms of post processing software, requiring additional manual labor and time in order to increase examination accuracy.

In this dissertation the goal is to optimize the workflow of fMRU imaging by eliminating the need for manual manipulation in the post-processing stage, leading to increased scanning efficiency. This experiment was done in a computer based simulation involving 100 virtual patients, each patient represented by an fMRU dataset containing 60 images of a kidney in motion being injected with contrast agent. The program automatically identifies the kidney including its substructures, measuring increases in contrast agent concentration while stabilizing and correcting for breathing motion. Resulting data was compared to input time-intensity-curves from which the difference was evaluated statistically by means of the Wilcox-Signed-Rank test for 50 kidneys with and 50 without movement correction. In the last step, Bonferroni correction was used to account for multiple testing.

Results successfully reflect the hypothesis where no significant difference was measured between observation and model data in the motion tracking group (mean z-score: -0.8) while significant difference was calculated in the non-motion-tracking-group (mean z-score: -3.2). Mean sum of differences between predicted and observed intensities across all kidneys and compartments was 0,072 with and 7,3 without movement correction, signifying good agreement between theoretical model and observed intensity changes.

Compared to previous methods of manual post-processing, we present an automated approach to fMRU imaging where additional labor from physicians or technicians becomes redundant. With further development, this could save valuable time by streamlining the image post-processing, making it possible to reduce costs and evaluate additional scans in the same timeframe. In relation to methods utilizing respiratory gating, our method allows for an

increase in information yield, giving the evaluating physician the ability to perform more specific and accurate diagnosis.

As a proof of principle dissertation, several parameters of this simulation had to be reduced in their level of complexity to allow for solid measurements. This way the obstacles of complex kidney anatomy and multiple background objects could be overcome without exceeding a limited timeframe. Inevitably, future research in this field would involve experiments with an increased level of detail, closing the gap between computer based simulation and real world imaging applications.

6. Literature

1. Silbernagl S, Despopoulos A. Taschenatlas Physiologie. Stuttgart [u.a.]: Thieme [u.a.]; 2007.

2. Schünke M, Schulte E, Schumacher U. Prometheus LernAtlas der Anatomie. Stuttgart: Thieme; 2012.

3. Herold G. Innere Medizin 2012: eine vorlesungsorientierte Darstellung; unter Berücksichtigung des Gegenstandskataloges für die Ärztliche Prüfung; mit ICD 10-Schlüssel im Text und Stichwortverzeichnis. Köln: Herold; 2012.

4. Understanding urine tests - National Library of Medicine - PubMed Health. 2013. Available from: http://www.ncbi.nlm.nih.gov/pubmedhealth/PMH0010405/#i684.s3

5. Price CP, Newall RG, Boyd JC. Use of Protein:Creatinine Ratio Measurements on Random Urine Samples for Prediction of Significant Proteinuria: A Systematic Review. Clin Chem. 2005 Sep 1;51(9):1577–86.

6. The Renal Association - CKD eGUIDE [Internet]. Proteinuria. Available from: http://www.renal.org/whatwedo/InformationResources/CKDeGUIDE/Proteinuria.aspx

7. Hahn T, Yao S, Dunford LM, Thomas J, Lohr J, Arora P, et al. A Comparison of Measured Creatinine Clearance versus Calculated Glomerular Filtration Rate for Assessment of Renal Function before Autologous and Allogeneic BMT. Biol Blood Marrow Transplant. 2009 May;15(5):574–9.

8. Soares AA, Eyff TF, Campani RB, Ritter L, Camargo JL, Silveiro SP. Glomerular filtration rate measurement and prediction equations. Clin Chem Lab Med. 2009 Sep 1;47(9):1023–32.

9. Madero M, Sarnak MJ. Creatinine-based formulae for estimating glomerular filtration rate. Curr Opin Nephrol Hypertens. 2011 Nov;20(6):622–30.

10. Ritchie G, Wilkinson AG, Prescott RJ. Comparison of differential renal function using technetium-99m mercaptoacetyltriglycine (MAG3) and technetium-99m dimercaptosuccinic acid (DMSA) renography in a paediatric population. Pediatr Radiol. 2008 Aug;38(8):857–62.

11. Werner MK, Schmidt H, Schwenzer NF. MR/PET: a new challenge in hybrid imaging. AJR Am J Roentgenol. 2012 Aug;199(2):272–7.

12. Evert J Blink. mri : physics [Internet]. [cited 2014 Sep 22]. Available from: http://www.mri-physics.net/textuk.html

13. Joseph P. Hornak. The Basics of MRI [Internet]. [cited 2014 Sep 22]. Available from: http://www.cis.rit.edu/htbooks/mri/inside.htm

14. Chang KJ, Kamel IR, Macura KJ, Bluemke DA. 3.0-T MR Imaging of the Abdomen: Comparison with 1.5 T1. Radiographics. 2008 Nov 1;28(7):1983–98.

15. Leyendecker JR, Barnes CE, Zagoria RJ. MR Urography: Techniques and Clinical Applications1. Radiographics. 2008 Jan 1;28(1):23–46.

16. Silverman SG, Leyendecker JR, Amis ES Jr. What is the current role of CT urography and MR urography in the evaluation of the urinary tract? Radiology. 2009 Feb;250(2):309–23.

17. Nikken JJ, Krestin GP. MRI of the kidney-state of the art. Eur Radiol. 2007 Nov;17(11):2780–93.

18. Renal Scintigraphy - Nuclear medicine imaging/scanning of the kidneys [Internet]. Renal Scintigraphy - Nuclear medicine imaging/scanning of the kidneys. Available from: http://www.radiologyinfo.org/en/info.cfm?pg=renal

19. Nolte-Ernsting CC, Tacke J, Adam GB, Haage P, Jung P, Jakse G, et al. Diuretic-enhanced gadolinium excretory MR urography: comparison of conventional gradient-echo sequences and echo-planar imaging. Eur Radiol. 2001;11(1):18–27.

20. Razavi SA, Sadigh G, Kelly AM, Cronin P. Comparative effectiveness of imaging modalities for the diagnosis of upper and lower urinary tract malignancy: a critically appraised topic. Acad Radiol. 2012 Sep;19(9):1134–40.

21. Verma S, Rajesh A, Prasad SR, Gaitonde K, Lall CG, Mouraviev V, et al. Urinary Bladder Cancer: Role of MR Imaging. Radiographics. 2012 Mar 1;32(2):371–87.

22. Hadjidekov G, Hadjidekova S, Tonchev Z, Bakalova R, Aoki I. Assessing renal function in children with hydronephrosis - additional feature of MR urography. Radiol Oncol. 2011 Dec;45(4):248–58.

23. Khrichenko D, Darge K. Functional analysis in MR urography - made simple. Pediatr Radiol. 2010 Feb;40(2):182–99.

24. Lee M-J, Kim M-J, Yoon C-S, Song SY, Park K, Kim WS. The T2-Shortening Effect of Gadolinium and the Optimal Conditions for Maximizing the CNR for Evaluating the Biliary System: a Phantom Study. Korean J Radiol. 2011;12(3):358–64.

25. Grattan-Smith JD, Little SB, Jones RA. MR urography in children: how we do it. Pediatr Radiol. 2008 Jan;38 Suppl 1:S3–17.

26. Brief Description of Patlak Analysis [Internet]. Vascular Permeability Analysis. Available from: http://www.vascularpermeability.org.uk/patlak.php

27. Hackstein N, Heckrodt J, Rau WS. Measurement of single-kidney glomerular filtration rate using a contrast-enhanced dynamic gradient-echo sequence and the Rutland-Patlak plot technique. J Magn Reson Imaging. 2003;18(6):714–25.

28. Grenier N, Mendichovszky I, de Senneville BD, Roujol S, Desbarats P, Pedersen M, et al. Measurement of Glomerular Filtration Rate With Magnetic Resonance Imaging: Principles, Limitations, and Expectations. Semin Nucl Med. 2008 Jan;38(1):47–55.

29. Darge K, Anupindi SA, Jaramillo D. MR Imaging of the Abdomen and Pelvis in Infants, Children, and Adolescents. Radiology. 2011 Oct 1;261(1):12–29.

30. Cheng PM, Moin P, Dunn MD, Boswell WD, Duddalwar VA. What the radiologist needs to know about urolithiasis: part 1--pathogenesis, types, assessment, and variant anatomy. AJR Am J Roentgenol. 2012 Jun;198(6):W540–7.

31. Copelovitch L. Urolithiasis in Children: Medical Approach. Pediatr Clin North Am. 2012 Aug;59(4):881–96.

32. Sudah M, Vanninen R, Partanen K, Heino A, Vainio P, Ala-Opas M. MR urography in evaluation of acute flank pain: T2-weighted sequences and gadolinium-enhanced three-dimensional FLASH compared with urography. Fast low-angle shot. AJR Am J Roentgenol. 2001 Jan;176(1):105–12.

33. Blandino A, Gaeta M, Minutoli F, Salamone I, Magno C, Scribano E, et al. MR urography of the ureter. AJR Am J Roentgenol. 2002 Nov;179(5):1307–14.

34. Takahashi N, Kawashima A, Glockner JF, Hartman RP, Kim B, King BF. MR urography for suspected upper tract urothelial carcinoma. Eur Radiol. 2009 Apr;19(4):912–23.

35. Darge K, Riedmiller H. Current status of vesicoureteral reflux diagnosis. World J Urol. 2004 Jun;22(2):88–95.

36. Darge K. Voiding urosonography with US contrast agents for the diagnosis of vesicoureteric reflux in children. Pediatr Radiol. 2008 Jan 1;38(1):54–63.

37. Snow BW, Taylor MB. Non-invasive vesicoureteral reflux imaging. J Pediatr Urol. 2010 Dec;6(6):543–9.

38. Sahay M. Congenital anomalies of kidney and urinary tract (CAKUT). Clin Queries Nephrol. 2013 Oct;2(4):156–65.

39. Renkema KY, Winyard PJ, Skovorodkin IN, Levtchenko E, Hindryckx A, Jeanpierre C, et al. Novel perspectives for investigating congenital anomalies of the kidney and urinary tract (CAKUT). Nephrol Dial Transplant. 2011 Dec 1;26(12):3843–51.

40. Payabvash S, Kajbafzadeh A-M, Saeedi P, Sadeghi Z, Elmi A, Mehdizadeh M. Application of magnetic resonance urography in diagnosis of congenital urogenital anomalies in children. Pediatr Surg Int. 2008 Sep;24(9):979–86.

41. Eurotransplant Statistics 2012 [Internet]. Year statistics 2012. Available from: http://www.eurotransplant.org/cms/mediaobject.php?file=year_2012.pdf

42. El-Diasty TA, El-Ghar MEA, Shokeir AA, Gad HM, Wafa EW, El-Azab ME, et al. Magnetic resonance imaging as a sole method for the morphological and functional evaluation of live kidney donors. BJU Int. 2005 Jul;96(1):111–6.

43. Elsayes KM, Menias CO, Willatt J, Azar S, Harvin HJ, Platt JF. Imaging of renal transplant: utility and spectrum of diagnostic findings. Curr Probl Diagn Radiol. 2011 Jun;40(3):127–39.

44. Blondin D, Koester A, Andersen K, Kurz KD, Moedder U, Cohnen M. Renal transplant failure due to urologic complications: Comparison of static fluid with contrast-enhanced magnetic resonance urography. Eur J Radiol. 2009 Feb;69(2):324–30.

45. Rees O, Agarwal SK. Nephrogenic systemic fibrosis: UK survey of the use of gadolinium-based contrast media. Clin Radiol. 2010 Aug;65(8):636–41.

46. European Society of Urogenital Radiology (ESUR)Guidelines [Internet]. Available from: http://www.esur.org/guidelines/

47. Jung J-W, Kang H-R, Kim M-H, Lee W, Min K-U, Han M-H, et al. Immediate Hypersensitivity Reaction to Gadolinium-based MR Contrast Media. Radiology. 2012 May 1;112025.

48. Shellock FG. Biomedical implants and devices: Assessment of magnetic field interactions with a 3.0-Tesla MR system. J Magn Reson Imaging. 2002;16(6):721–32.

49. Planert J, Modler H, Vosshenrich R. Measurements of magnetism-related forces and torque moments affecting medical instruments, implants, and foreign objects during magnetic resonance imaging at all degrees of freedom. Med Phys. 1996 Jun 1;23(6):851–6.

50. Information About Radiation from Diagnostic Imaging Procedures [Internet]. University of Pennsylvania; Available from: http://www.ehrs.upenn.edu/media_files/docs/pdf/websiteinfo%282%29.pdf

51. Claudon M, Durand E, Grenier N, Prigent A, Balvay D, Chaumet-Riffaud P, et al. Chronic urinary obstruction: evaluation of dynamic contrast-enhanced MR urography for measurement of split renal function. Radiology. 2014 Dec;273(3):801–12.

52. Delgado J, Bedoya MA, Adeb M, Carson RH, Johnson AM, Khrichenko D, et al. Optimizing functional MR urography: prime time for a 30-minutes-or-less fMRU. Pediatr Radiol. 2015 Mar 20;

53. Darge K, Grattan-Smith JD, Riccabona M. Pediatric uroradiology: state of the art. Pediatr Radiol. 2011 Jan;41(1):82–91.

54. Zhang JL, Morrell G, Rusinek H, Sigmund EE, Chandarana H, Lerman LO, et al. New magnetic resonance imaging methods in nephrology. Kidney Int. 2014 Apr;85(4):768–78.

55. Jaimes C, Darge K, Khrichenko D, Carson RH, Berman JI. Diffusion tensor imaging and tractography of the kidney in children: feasibility and preliminary experience. Pediatr Radiol. 2014 Jan;44(1):30–41.

56. Delgado J, Toro R, Rascovsky S, Arango A, Angel GJ, Calvo V, et al. Chloral hydrate in pediatric magnetic resonance imaging: evaluation of a 10-year sedation experience administered by radiologists. Pediatr Radiol. 2015 Jan;45(1):108–14.

57. Chavhan GB, Babyn PS, Vasanawala SS. Abdominal MR imaging in children: motion compensation, sequence optimization, and protocol organization. Radiogr Rev Publ Radiol Soc N Am Inc. 2013 May;33(3):703–19.

58. Stephan KE, Harrison LM, Penny WD, Friston KJ. Biophysical models of fMRI responses. Curr Opin Neurobiol. 2004 Oct;14(5):629–35.

59. Attenberger UI, Sourbron SP, Michaely HJ, Reiser MF, Schoenberg SO. Retrospective respiratory triggering renal perfusion MRI. Acta Radiol Stockh Swed 1987. 2010 Dec;51(10):1163–71.

60. Lim JS. Two-dimensional signal and image processing. Prentice Hall; 1990. 720 p.

61. Microsoft Windows Bitmap Format [Internet]. BMP.TXT. Available from: http://www.fileformat.info/format/bmp/spec/e27073c25463436f8a64fa789c886d9c/view.htm

62. Gibbons JD. Nonparametric statistical inference. Boca Raton: Chapman & Hall/Taylor & Francis; 2011.

63. Streiner DL, Norman GR. Correction for multiple testing: is there a resolution? Chest. 2011 Jul;140(1):16–8.

64. Othman S, Al-Hawas A, Al-Maqtari R. Renal Cortical Imaging in Children: 99mTc MAG3 Versus 99mTc DMSA. Clin Nucl Med April 2012. 2012;37(4):351–5.

65. Gerig G, Kikinis R, Kuoni W, von Schulthess GK, Kübler O. Semiautomated ROI analysis in dynamic MR studies. Part I: Image analysis tools for automatic correction of organ displacements. J Comput Assist Tomogr. 1991 Oct;15(5):725–32.

66. de Priester JA, Kessels AGH, Giele EL., Boer JA den, Christiaans MHL, Hasman A, et al. MR renography by semiautomated image analysis: Performance in renal transplant recipients. J Magn Reson Imaging. 2001 Aug 1;14(2):134–40.

67. Holland AE, Goldfarb JW, Edelman RR. Diaphragmatic and cardiac motion during suspended breathing: preliminary experience and implications for breath-hold MR imaging. Radiology. 1998 Nov 1;209(2):483–9.

68. Giele EL, de Priester JA, Blom JA, Boer JA den, van Engelshoven JM, Hasman A, et al. Movement correction of the kidney in dynamic MRI scans using FFT phase difference movement detection. J Magn Reson Imaging JMRI. 2001 Dec;14(6):741–9.

69. Sun Y, Moura J, Yang D, Ye Q, Ho C. Kidney segmentation in MRI sequences using temporal dynamics. In: 2002 IEEE International Symposium on Biomedical Imaging, 2002 Proceedings. 2002. p. 98–101.

70. Sun Y, Jolly M-P, Moura JMF. Integrated registration of dynamic renal perfusion MR images. In: 2004 International Conference on Image Processing, 2004 ICIP ’04. 2004. p. 1923–6 Vol. 3.

71. Sun Y, Moura JMF, Ho C. Subpixel registration in renal perfusion MR image sequence. In: IEEE International Symposium on Biomedical Imaging: Nano to Macro, 2004. 2004. p. 700–3 Vol. 1.

72. Rusinek H, Boykov Y, Kaur M, Wong S, Bokacheva L, Sajous JB, et al. Performance of an automated segmentation algorithm for 3D MR renography. Magn Reson Med. 2007 Jun 1;57(6):1159–67.

73. Tang Y, Jackson H, Lee S, Nelson M, Moats RA. Shape-aided kidney extraction in MR urography. Conf Proc Annu Int Conf IEEE Eng Med Biol Soc IEEE Eng Med Biol Soc Conf. 2009;2009:5781–4.

74. Tang Y, Jackson H, De Filippo R, Nelson M, Moats R. Automatic renal segmentation applied in pediatric MR Urography. Int J Intell Inf Process. 2010 Sep 30;1(1):12–9.

75. Merrem AD, Zöllner FG, Reich M, Lundervold A, Rorvik J, Schad LR. A variational approach to image registration in dynamic contrast-enhanced MRI of the human kidney. Magn Reson Imaging. 2013 Jun;31(5):771–7.

76. Chefd'hotel C, Hermosillo G, Faugeras O. A variational approach to multi-modal image matching. In: IEEE Workshop on Variational and Level Set Methods in Computer Vision, 2001 Proceedings. 2001. p. 21–8.

7. Appendix

Abstract

Introduction: Functional magnetic resonance urography is a frequently carried out examination in pediatric radiology. This usually involves respiration gated dynamic T1w sequences after i.v. administration of Gadolinum contrast agents. Breathing motion is a challenge to analysis of imaging time series in many settings, especially in thorax and abdomen. We investigated in a software phantom as proof of principle, whether object recognition based tracking is capable of intensity-time-curve analysis.

Materials and Methods: Images-time-series (no respiratory gating) of 100 kidneys were artificially generated (Matlab, TheMathworks, Natick, NA, USA). Respiratory movement was implemented by a sinusoidal coordinate shift with an amplitude of 3 cm and frequency of about 6 min^{-1}. Renal intensity changes after contrast application were modeled using gamma functions for three anatomical compartments: cortex, pyramids and renal pelvis. Movement correction was carried out for half of the study population. Intensity-time-curves were extracted using automatically placed regions of interest relative to central coordinates of the kidney on the first image. Intensity changes over time extracted from the ROIs were subtracted from known intensity changes of the software model. Differences were assessed using Wilcox-Signed-Rank test for 50 kidneys with and 50 without movement correction. We used Bonferroni method to correct for multiple testing.

Results: Mean sum of differences between predicted and observed intensities across all kidneys and compartments was 0,072 with and 7,3 without movement correction. Significant difference between observation and model was not seen in any compartments of the tracking group (mean z-score: -0.8), whereas there was in 66 compartments in the non-tracking group (mean z-score: -3.2), signifying good agreement between theoretical model and observed intensity changes with object recognition-based tracking, and suboptimal agreement in the non-tracking-group due to movement artifacts.

Discussion: We conclude that object-recognition based anatomical tracking is feasible in fMRU as an alternative or addition to respiration gating. This may allow a higher temporal resolution of these studies in the future. In our experiments, additional assessment of the renal parenchyma's substructures cortex and pyramids was possible.